LAWRENCE
LIVERMORE
NATIONAL
LABORATORY

UCRL-JRNL-222298

First Wall and Operational Diagnostics

C.J. Lasnier, S.L. Allen, J.A. Boedo, M. Groth, N.H. Brooks, A. McLean, B. LaBombard, J.P. Sharpe, C.H. Skinner, D.G. Whyte, D.L. Rudakov, W.P. West, C.P.C. Wong

June 21, 2006

Fusion Science and Technology

Disclaimer

First wall and operational diagnostics

C.J. Lasnier[a)], S.L. Allen[a)], J.A. Boedo[b)], M. Groth[a)], N.H. Brooks, A. McLean[c)], B. LaBombard[d)], J.P. Sharpe[e)], C.H. Skinner[f)], D.G. Whyte[g)], D.L. Rudakov[b)], W.P. West, C.P.C. Wong

General Atomics, P.O. Box 85608, San Diego, California 92186-5608, USA

[a)]Lawrence Livermore National Laboratory, Livermore, California

[b)]University of California, San Diego, California, USA

[c)]University of Toronto, Toronto, Canada,

[d)]Massachusetts Institute of Technology,

[e)]Idaho National Laboratory

[f)]Princeton Plasma Physics Laboratory,

[g)]University of Wisconsin

Contact author: C.J. Lasnier, General Atomics, P.O. Box 85608, San Diego, California 92186-5608, Phone (858) 455-4150, Fax (858) 455-4156, e-mail: Lasnier@fusion.gat.com

Total pages: ?? (?? text, ? figures, ? tables)

(Received

ABSTRACT: In this chapter we review numerous diagnostics capable of measurements at or near the first wall, many of which contribute information useful for safe operation of a tokamak. There are sections discussing infrared cameras, visible and

VUV cameras, pressure gauges and RGAs, Langmuir probes, thermocouples, and erosion and deposition measurements by insertable probes and quartz microbalance. Also discussed are dust measurements by electrostatic detectors, laser scattering, visible and IR cameras, and manual collection of samples after machine opening. In each case the diagnostic is discussed with a view toward application to a burning plasma machine such as ITER.

I. INTRODUCTION, ORGANIZATION

In this chapter we review diagnostics that make measurement at or near the wall, and may provide useful information for safe operation of a burning plasma tokamak. We discuss each diagnostic with a view toward the usefulness and challenges of application of that diagnostic for ITER. The organization scheme is listed below.

I. IR Camera Measurements

II. Visible/VUV TV

III. Pressure Gauges and RGA

- A. PRESSURE MEASUREMENTS
- B. ASDEX ionization gauge
- C. Partial pressure measurements with an RGA

IV. Probe Measurements

- A. Divertor Langmuir Probes (FMP)
- B. Limiter particle flux probes
- C. Outer scanning probe (ASP)
- D. Vertical scanning probe (FSP)
- E. Inner scanning probe (ISP)

V. Thermocouples for heat flux measurement

VI. EROSION and DEPOSITION MEASUREMENTS

- A. DIMES EROSION AND DEPOSITION MEASUREMENTS
- B. Quartz microbalance

VII. DUST MEASUREMENTS

- A. Importance of dust; electrostatic dust detectors
- B. Thomson Scattering dust measurements
- C. Visible and IR measurements
- D. Dust analysis of manual samples after machine opening

I. IR CAMERA MEASUREMENTS

Infrared thermography is used in tokamaks to measure the surface temperature of plasma facing components, calculate the heat flux deposited there by plasma interaction and absorbed radiation, and warn of dangerously high surface temperatures[1]. Typically an infrared camera is used to view blackbody emission through a vacuum window. Sapphire has adequate window transmission to wavelengths as long as five μm. For cameras operating in the 8-12 μm region, zinc selenide may be used.

Due to the shift in the peak of the blackbody spectrum with temperature, the commonly available 3-5 μm detectors are not as sensitive for temperature measurements of objects near room temperatures as 8-12 μm cameras. For elevated divertor plate temperatures seen near the strike points in tokamaks, the 3-5 μm cameras provide good signal levels, while the 8-12 μm cameras continue to perform well. Usually it is necessary to look through plasma in order to make the measurement. At wavelengths shorter than 3 μm, molecular emission lines from intervening plasma can complicate attempts to view interior components.

Thermography systems for tokamak physics may be thought of in two classes: slow and fast. The slow systems measure time-averaged surface temperatures at tens to hundreds of images per second, ideally for the full duration of a plasma pulse and with high spatial resolution. The fast systems are for measurement of thermal energy deposited by transients such as ELMs and disruptions. A practical minimum for these measurements is 10,000 profiles per second. This is marginally sufficient and higher speed is very desirable. Typically the fast camera does not provide full frames at that rate, only lines or sub-windows. In some cases the same instrument supplies the fast and slow functions, perhaps simultaneously.

If a digital infrared camera is used on a plasma device generating significant neutron radiation, shielding will be required for the camera. Digital cameras contain large numbers of small transistors that are susceptible to neutron damage. Magnetic and/or rf shielding may also be required to reduce noise interference that can prevent normal operation of the camera.

It is desirable to minimize the number of mirrors in the IR system to reduce transmission losses. Mirrors should be front-surface reflectors. Extremely high surface quality is not needed for good infrared images, but a decent image quality at visible wavelengths is helpful in aligning the system. If the system contains lenses, germanium may be used as the lens material for high refractive index and reasonable transmission. To optically align the system, germanium lenses must be removed since they do not transmit visible light.

A primary challenge for use of thermography on a burning plasma experiment is, as for many other diagnostics, survival of the optical component nearest the plasma, which perhaps must be a mirror. Because of the long wavelength, mirrors that have an imperfect surface finish incapable of forming a visible-light image may still function in the infrared. Signal losses may still increase on such a damaged surface.

Vacuum windows and optics contribute their own infrared radiation, which decreases the signal-to-noise ratio of the diagnostic. To minimize this, the temperatures of the window and optics need to be controlled. For a long-pulse plasma device, particularly a burning-plasma machine, this will require active cooling. Care must be taken that cooled in-vacuum components do not become condensation points for re-deposited material.

Both analog video and digital cameras have been used with appropriate data acquisition systems for tokamak IR measurements. It is important to have timestamps for the frames, which fix the time of the data relative to other diagnostics. For the DIII-D

digital cameras, the first two 16-bit pixels of each image are replaced by a 32-bit count representing the number of microseconds since trigger time.

It is a great advantage to use a data acquisition system that can operate unattended and store the data in such a way that it is easily associated with the correct plasma pulse. A near-real-time estimate of the heat flux is also useful. The challenges of capturing, storing, and viewing IR data from very long plasma pulses such as those expected in ITER, is very different from the requirements for the relatively short-pulse machines, which predominate as of this writing.

The maximum data rate from fast infrared cameras is increasing with new development. State-of-the art data acquisition is required to keep up with a fast camera, and decisions must be made on how to store the enormous amount of data from long-pulse discharges or how to selectively save parts of it.

In order to provide useful temperature and heat flux data, the camera systems must be calibrated. Commercial cameras are available with thermographic calibrations, but these calibrations are typically not useful because the windows, mirrors, and lenses that may be used in the tokamak application were not included. It is therefore necessary to calibrate the system as part of the implementation and maintenance.

In DIII-D, IR camera calibration is accomplished in situ by recording camera data when the vacuum vessel is baked. Thermocouple data from sensors embedded in plasma facing tiles inside the tokamak are simultaneously recorded, and calibration curves are fitted to temperature vs. signal plots. This has the advantage of providing a front-to-back calibration. Another approach is to measure the transmission of individual components to arrive at a transfer function of the whole system. This has the potential advantage of easy replacement of components without recalibrating the whole system, at the likely cost of accumulated error from each of the transmission measurements.

A third scheme relies on removing all the IR system components from the tokamak (including the window, or a facsimile), assembling them on a bench with the same alignment, and viewing a calibrated blackbody source. Some systems are quite sensitive to the alignment of components, which may be difficult to reproduce exactly on the bench.

It is also possible to install an independently-heated object inside the vessel to avoid having to bake the entire vessel for a camera calibration. Plasma coating of windows is less problematic for infrared measurements than for visible wavelengths, but should be taken into account for the calibration. The signal level emitted from carbon tiles approaches 90% of the blackbody emission of the same temperature. Metal tiles have lower emissivity, which must be considered in the system design and data analysis. The amount of infrared light reflected from the tile surfaces of interest must be small compared to the thermal emission from the tile, else then analysis is excessively complicated. This criterion will be difficult to meet if a hot object is reflected in a lower-temperature surface whose temperature we wish to measure.

Spatial calibrations must also be maintained so that correct profiles can be plotted. Such calibrations may be obtainable by inspecting images for landmarks at known locations, or perhaps by using an initial in-vessel alignment target if the alignment of the optics is sufficiently stable. A permanent in-vessel alignment and spatial calibration target is helpful, particularly for systems whose sensitivity does not allow viewing of the vessel interior at normal non-operating temperature.

Once calibrated surface temperature data is available, we wish to calculate the heat flux. The result of this calculation is model dependent, and includes assumptions about the thermal conductivity and capacity of the tiles, whether these quantities vary with temperature (important for high power and long pulses), whether they are isotropic, and

whether the heat is assumed to propagate in one direction (into the tile perpendicular the surface), in two dimensions (perpendicular and parallel to the surface in one direction), or in three dimensions so as to incorporate edge effects and the true geometry of the tiles. Additional approximations are sometimes made, such as a semi-infinite 1-D model, which assumes the tile is infinitely thick. This calculation is fast to perform but suffers decreasing accuracy for long pulses, where the back of the tile begins to heat up and affect the heat propagation.

For the analysis of fast heat pulses such as ELMs and disruptions, there are additional complications. In many cases, the apparent surface temperature drops more rapidly after an event than can be accounted for by conduction into the bulk material or radiation. This gives rise to the calculation of a negative heat flux when a simple model is applied. Various authors have proposed that this may be due to a thin surface layer of differing thermal properties[2], and have used ad-hoc surface layers in their models with thermal properties adjusted to minimize the negative overshoot in the calculated heat flux. The heat flux calculated from measured surface temperature can be integrated over the radial profile, and with the assumption of toroidal symmetry, the total power to the divertor plate can be estimated. This can be used to monitor power balance for the plasma. The width and maximum value of the heat flux deposition on a divertor plate provides a measurement of the energy flowing in the scrape-off layer. Among other applications, infrared cameras have been used to show desirable heat flux reduction in a radiative divertor[3-5], and to explore anomalous heat flux deposition during QH-modes that may be due to elevated ion losses[6].

One example of the type of measurements possible with an IRTV system is the balance of power between upper and lower divertors in the double-null configuration (ELMing H-mode with no radiative divertor). The magnetic configuration varied continuously between two states during a shot. The first state was essentially lower

single-null and the second was nearly upper single-null. (The control system was not adjusted far enough to make a true upper SN.) The separatrix associated with one null occurred on a flux surface that mapped at the midplane to smaller minor radius than the separatrix of the other null. The divertor magnetically connected to the inner flux surfaces intercepted most of the heat before the energy could be transported across field lines to the outer flux surfaces connected to the other divertor. The intermediate states occurred with decreasing distance between the two separatrices at the magnetic midplane, D_{rsep}. The control system maintained D_{rsep} within ±2 mm of the desired value, according to the EFIT code output.

For the magnetically balanced case, the two nulls lay on the same flux surface. However, this did not correspond to balanced heat flux between the two divertors (Fig. 1). This could be due to a systematic offset in the EFIT calculation of the X–point locations and the flux values. The offset in the heat flux balance with respect to the magnetic balance might also be due to particle $\tilde{N}\mathbf{B}$ drifts. Note that the transition between all heat flux to the upper divertor and all to the lower is smooth and controllable, according to these data. This bodes well for future attempts to share power loading equally between upper and lower divertors.

Technology for infrared camera detectors is changing rapidly, in part because of increasing industrial, military, and security demand for infrared cameras. In addition to the liquid-nitrogen cooled HgCdTe (sometimes called MCT) and InSb detectors available in the past, room-temperature micro-bolometer arrays are now commercially available, as are QWIP (quantum well infrared photodetector or photoconductor). The QWIP detectors are cooled and highly sensitive, and generally both more expensive and more sensitive than the microbolometers. This may be seen by comparing the NEDT (noise equivalent δT) specification for the cameras, where smaller is better. Most cameras now available

use fixed arrays of detectors, whereas older cameras sometimes used a single detector with scanning mirrors.

Microbolometer measurements are better suited to slow measurements than fast, since they rely on bulk heating of a small volume of material in the detector. The other detectors mentioned here may be run at high speed if sufficient light is available. Other detector technologies are under development and will no doubt appear on the commercial market in the next few years.

Cooled detectors are available in both in cameras with liquid nitrogen reservoirs and in instruments with tiny closed-loop helium mechanical refrigeration units. The expected life-cycle of the refrigeration unit should be compared with the required operating lifetime. Cooled cameras require a few minutes to stabilize after cooling is started, depending largely on the thermal mass to be cooled. Microbolometer cameras can also benefit from allowing thermal equilibrium to be established after turn-on.

Very little data is available concerning the effect of high levels of radiation on these cameras, particularly of the spectrum of gamma and neutron energies in a fusion device. It is virtually certain that in a burning-plasma device, the camera will require shielding against neutrons, gamma rays, magnetic fields, and electromagnetic noise. The usual close attention must be paid to proper grounding.

It is not necessary to use a multi-sensor camera to obtain useful thermographic information. Commercially available products include infrared thermometers and pyrometers, as well as discrete stand-alone detectors. These devices still need and use optics to focus infrared light from a target area onto the detector. Commercial systems are typically slow, but a custom system can be very fast. Similar considerations apply to the detector choice here as for cameras.

II. VISIBLE/VUV TV

Two-dimensional cameras have been employed in major fusion devices to measure the 3-D spatial distribution of emission from plasma species in the VUV and visible wavelength range (100-900 nm). Their application ranges from general surveillance of the vacuum vessel during plasma operation to wavelength-resolved measurements of the intensity distributions of emission in the scrape-off layer (SOL) plasma.

Visible light cameras are also useful to machine operators in monitoring safe operation, such as insuring that local hot spots are not glowing in visible light, and that no large chunks of debris are present inside the device. Smaller objects, which fall or are propelled into the plasma, may light up and be observed with the camera. These small objects are frequently benign, although if enough impurities are introduced a disruption may ensue.

The principal technology involved in plasma imaging is solid-state sensors, such as charge-coupled devices (CCDs), charge-injection devices (CIDs), and complementary metal-oxide semiconductors (CMOS). While in CCD and CMOS sensors quantum efficiencies close to unity and dynamic resolution >12 bits have been achieved, these sensors are highly susceptible to damage from or noise induced by neutron and gamma emission naturally present in fusion devices. CID sensors employed in the tokamaks DIII-D[7] and JET[8] have been shown to operate reliably in fusion devices including resistance to neutron fluxes and electromagnetic radiation, but their performance can be significantly degraded when exposed to extremely high neutron fluences (in JET $\sim 1\times 10^{13} n/cm^2$). The main disadvantage of CID cameras for tokamak application is their sensitivity to magnetic fields.

High-speed CCD cameras have been used in tokamaks, usually in the form of a commercial camera that stores digital images in on-board memory, which is read out after the discharge is over. This technique is hardly suitable for long-pulse experiments except for the analysis of brief intervals containing transient behavior of interest.

Visible camera in use today most commonly are still are analog video cameras. The video may be recorded on tape and/or saved digitally using a frame grabber in a computer. There are many digital visible cameras available, some of which have the required speed and resolution. These may become more commonly used in fusion experiments in the near future. The increased use of highly integrated digital circuitry in such cameras makes them more susceptible to radiation damage and makes the necessity of radiation shielding doubly important. Some cameras are sensitive to magnetic fields, and so care must be taken to shield them or place them in safe locations. It is apparent that the trend toward fast and higher-resolution commercial cameras will continue. This is primarily a matter of integrating new and faster functions, and not of developing new types of detectors.

Because of the need of shielding of the sensors from neutron and gamma emission, and from electromagnetic fields, optical lens/mirror systems or fiber image guide technology are employed to relay the light collected with lenses at the viewport to the sensor. Depending on the sensor, this involves transmission of light over distances of several meters. If fiber image guides are to be used in future burning plasma experiments, development of radiation hardened optical components is needed to prevent signal attenuation in the material due to creation of color centers (attenuation proportional to neutron fluence).

The same process of radiation damage can occur in lenses, although the effect is smaller because of the shorter optical path length through a lens compared to a fiber

guide. Lenses may also be more easily made of radiation-tolerant material than a fiber guide. Other challenges in a burning plasma experiment include stability of optical alignment in the presence of large temperature changes and thermal gradients, and protection of in-vessel optics by shutters. Shutters may be less effective in long-pulse devices since the intervals during which the shutter is open will also be long.

Camera views may be calibrated by putting a light source of known intensity into the vacuum vessel before evacuation. Vignetting may be quantified using an extended source of uniform luminance, or a smaller moveable source. Spatial calibration is also necessary and may be accomplished by use of a temporary alignment target inside the device. These techniques will not be practical in a highly activated machine, so other measures for in-situ calibration must be devised. In the case of a camera view using a fiber image guide, regular calibrations of the image guide transmission at wavelengths of interest are useful in quantifying the darkening due to radiation damage. If cameras or optics need to be regularly removed from the machine, a means of replacing them exactly in the pervious alignment is necessary so that the calibrations remain valid.

Camera views in present fusion devices range from wide-angle tangential views of the entire vacuum vessel (e.g., AUG, JET, NSTX) (Fig. 2) to collimated views of specific regions of the machine, where most of the emission occurs, e.g., the divertor (e.g., Alcator C-mod, AUG, DIII-D, JET, MAST, NSTX, TCV). The benefits of using camera systems over other techniques include large field-of-view, high spatial resolution, and a very large number of view chords permitting tomographic reconstruction of the image data. Vertical views are also used to obtain 3-D poloidal and toroidal distribution profiles across the divertor and main wall (e.g., NSTX, DIII-D). Wavelength resolved measurements of plasma radiation using filters and tangential views have allowed the 2-D poloidal emission profiles to be inferred from the image data[7,9-11], which has significantly advanced our understanding of scrape-off layer physics. Typical plasma neutral and ion

species monitored with wavelength interference filters are listed in Table 1, including hydrogen/deuterium and main plasma impurities. Measuring the spatial distribution of the emission helped to elucidate the role of volume recombination in divertor detachment[12-16] and density limit physics[14], and to measure intrinsic particle sources and interpret their transport into the core plasma[17]. Impurity emission is used to determine the location of the ionization zone in front of the divertor target (e.g., the contours of the CIII emission represents zones of electron temperatures of the order 8-10 eV). Recently in DIII-D, measurements of the emission from C^{1+} and C^{2+} ions in the main chamber following methane injection indicated anomalously large scrape-off layer flows in the direction of the high-field side divertor[18]. Use of cameras with an image intensifier coupled to a phosphor plate and a CID sensor[19], and the introduction of fast-framing CMOS devices in fusion devices[20-22] has permitted measurements of the spatial structure of the emission during microsecond-fast events, such as intermittent transport events[23-25], ELMs[20,22,26,27], and disruptions[28].

Two-dimensional imaging of VUV emission (155 nm)[29-32] has been used to verify the spatial distribution of the impurity species radiating the most power from the boundary plasma in present tokamaks with carbon impurities. The 155 nm VUV line emission from triply ionized carbon was imaged in the DIII-D tokamak using a series of MgF2 imaging relay lenses, a wavelength interference filter and a P1 phosphor plate all in a secondary vacuum chamber mounted on a tokamak port[29]. The secondary vacuum chamber served two purposes: 1) it eliminated the attenuation of the VUV emission in atmospheric pressure gases and 2) it isolated the relay optics system from the tokamak primary vacuum. The relay optics were designed to give an acceptable spot size for a well focused image at 155 nm but it was not possible to achieve good focusing for a broad range of wavelengths. The imaging was done outside the secondary vacuum with a standard CID based camera focused on the P1 phosphor plate. The system was designed to image the

VUV line of C^{3+} because spectroscopic measurements[33,34] had shown that it was the dominant power radiator from carbon in the DIII-D divertor. In principle the design approach could be optimized to look any other lines in the VUV wavelength range.

Comparison of the spatial profile of the high radiated power 155 nm C^{3+} emission with visible 465 nm C^{2+}emission showed that visible imaging can give a good indication of the location of the high radiation zones for various impurities[30-32]. Reconstructions of the 2D spatial profile of the CIV (155 nm) VUV emission and the CIII (465 nm) visible emission showed that for the DIII-D divertor with steep spatial gradients in electron temperature in the range of 5–20 eV, the CIII emission occurred in regions very close to the regions with strong CIV emission[30-32]. This was true for both attached and detached divertor plasma operation in DIII-D since the steep temperature gradients existed over the 5–20 eV range in both cases. Given that imaging of VUV emission is much more technically complicated that imaging of visible emission, these experiments provided valuable verification of the usefulness of visible emission imaging for determining the regions with high radiated power from partially ionized carbon.

III. PRESSURE GAUGES AND RGAs

A. Pressure measurements

Recycling of charged particles on the plasma-facing surfaces of the tokamak vacuum vessel leads to a continuous refueling of the confined plasma by neutral atoms. In tokamaks with window frame limiters[35], recycling of the fuel ions is concentrated in a single azimuthal plane; in divertor tokamaks, the recycling is spread out toroidally, but peaked poloidally on remotely located, divertor target plates. In either case, asymmetry in the neutral fueling source leads to pressure gradients in the annular volume surrounding the plasma column. Fast localized measurement of neutrals is required to understand the distribution of the fueling source and its effect on global confinement and plasma behavior. To this end, a variety of custom devices have been developed which operate in the multi-Tesla field produced by the magnetic coils encircling the toroidal vacuum vessel of the tokamak. Two electrical transducers for measuring total pressure will be described: these are the ASDEX ionization gauge and a modified Penning gauge.

Besides the fuel ion, a tokamak plasma may contain a variety of minority species. Foremost in importance is the hydrogen isotope tritium, since the nuclear reaction between the deuterium (D) and tritium (T) isotopes constitutes the energy-producing process in a fusion reactor. In experiments on JET and TFTR, tritium has been introduced into deuterium plasmas as a minority species to study the physics of reacting plasmas. The end product, or ash, of the D-T fuel cycle is helium; its removal of helium from the confined plasma is necessary to prevent dilution of the nuclear fuel. Studies of ash removal in existing tokamaks have been performed with atomic helium injected either as a gas or as beam of high energy neutrals. Other gases introduced as minority constituents

in present-day experiments include inert gases such as nitrogen, and noble gases such as neon, argon and krypton. Strong radiative emission from ions of these non-intrinsic impurities can reduce the specific heat load conducted to the divertor targets by electron thermal transport. However, the radiative loss by these impurity ions produces a beneficial effect only if the impurity is preferentially concentrated in the cold mantle and divertor. Measuring the partial pressure of these gases in the divertor pumping plenum has played a key role in evaluating the divertor concentration of these impurities. Partial pressures of all the species mentioned above --- tritium, helium, nitrogen, and noble gases --- have been measured by optical detection of their spectral emissions in commercial Penning gauges, discussed below.

Hydrocarbons (HCs) are another neutral species always present in tokamaks with graphite walls. Chemical sputtering of carbon surfaces by hydrogen atoms and ions produces a mixture of methane and heavier HCs. For studies of their production, transport and final disposition, the ability to measure partial pressures of HCs is essential. Residual Gas Analyzers (RGAs) have been found well-suited to the task. Special methods have been employed with RGAs for detecting HCs after tokamak pulses and during the glow discharge cleaning periods between pulses.

B. ASDEX ionization gauge

The ASDEX ionization gauge is a patented device[36] relying on the basic principles of a hot cathode, ionization gauge[37]. However, its geometric design is dictated by the need to operate in multi-Tesla magnetic fields which constrain charged particles to move in tight helical orbits about the field line direction. In the ASDEX gauge head, a linear arrangement of filament, control grid, acceleration grid and collector, along an axis parallel to the magnetic field, permits the use of small electrostatic fields to accelerate

electrons from the filament and to collect ions resulting from electron- neutral collisions, without impediment by the circular Larmor orbits. Alignment of the gauge axis with the tokamak field serves a second purpose: it confines the ions borne within the gauge volume from leaking out in the transverse direction and, thereby, improves the ion collection efficiency by almost an order of magnitude compared to operation without magnetic field.

The tokamak machine hall is an electrically noisy environment, due the use of many high current, rapidly pulsed power supplies on the magnetic coil and auxiliary heating systems. Amplification and detection of small currents, brought to a high state of perfection in commercial Bayard - Alpert gauge tubes, is not suitable for a real time tokamak diagnostic. In the ASDEX gauge head, a filament strong enough to withstand strong $J \times B$ forces is heated with a dc current of 10-15 A. With electron extraction from the filament square-wave modulated by the control grid voltage, phase-locked detection is used to measure the average ion current reaching the collector. Since ground loops are potentially disastrous in a measurement of low current, special care is taken with respect to electrical isolation of each bias supply; remote control from outside the machine hall is performed with full optical isolation.

Pressures of interest in a tokamak range from 10^{-6} Torr at the boundary of the core plasma to the low 10^{-2} torr range in the divertor plenums. The ASDEX gauge is operative over this entire range. Time resolution is generally between 1 and 10 ms, with the value for a particular gauge governed by geometric factors rather than the intrinsic response of the gauge itself. The gauge head measures the flux of particles, 1/4 n v, incident on the aperture in a sheet metal enclosure surrounding the head. The enclosure serves the secondary role of shielding the ionization gauge elements from ultraviolet light, which can cause photoelectron emission. Outside the core plasma, the atomic flux detected by the gauge head can be directly related to the charge-exchange neutral outflux across the

separatrix. In the divertor pumping plenums, it is common practice to place the gauge head out of direct view of the pumping plenum throat, such that the particles reaching the gauge aperture are deuterium molecules thermalized to the known temperature of the vessel wall. With the additional knowledge of the velocity of the particles entering the gauge aperture, the ionization gauge signal may be calibrated to yield the pressure in the pumping plenum.

On DIII-D, ASDEX gauges have been placed in divertor pumping plenums, the divertor private flux region and in the boundary outboard of the core plasma. The complete gauge system, including the ionization gauge head, the filament power supply, and the local and remote electronic control boxes, are obtained from a commercial supplier[38] which manufactures the diagnostic system under license from IPP-Garching.

The ASDEX gauges are calibrated against an absolute pressure sensor – a capacitive manometer[39]. On DIII-D these gauges are located a considerable distance outside the toroidal field coil cage, with low conductance tubing coupling them to the vacuum vessel. Consequently, they have a response time measured of the order of 100 ms. To calibrate the ASDEX gauges against the absolute pressure manometers, the DIII-D vacuum vessel is valved off from its pumping system and a series of deuterium gas pulses are injected so as to produce a staircase ramp in pressure. Each step of the ramp must be long enough for the pressure measured by the absolute manometer to approach an asymptotic level.

Total pressure measurements on tokamaks have also been performed with Penning gauges. These are cold cathode pressure gauges, which employ a magnetic field to create a mirror-like trap for confinement of ions borne inside them[39]. On the Alcator C-MOD two changes were performed to adapt the standard commercial style Penning gauge for use in the main chamber and in the divertor plenums of the tokamak. First, the external magnet which provides the axial field in a commercial Penning gauges was replaced with

the field generated by the tokamak's coils and plasma current. Second, the gauge head was miniaturized to fit in the limited space behind armor tiles. Though not quite as sensitive as ASDEX gauges, the Penning gauge is easily capable of measuring the mtorr pressures typical of the divertor plenum and private flux regions. The time response of the Penning gauge, like that of the ASDEX ionization gauge, is governed by geometric factors rather than the intrinsic response of the gauge itself.

Impurity concentrations in the plasma core are usually performed spectroscopically, by measuring the principal ionic charge states present in each radial-defined temperature zone and summing over the densities in these states. Comparable measurements of impurities in the divertor plasma are much more difficult to make, due to the complicated, two-dimensional variation in plasma temperature and density across the divertor region. For impurities which don't stick to the divertor targets, i.e., recycling impurities such as noble gases, the task is greatly simplified. These impurities can be extracted from the divertor target in gaseous form to a remotely located Penning gauge. Once neutralized, there is only one species of the impurity which needs to be measured. Emission lines of the neutral impurity atom excited by electron impact in a Penning gauge provides a unique spectral signature for each element[40].

Those familiar with commercial residual gas analyzers (RGAs) may wonder why a new technique was developed to measure the partial pressure of gases on tokamaks, given that most tokamaks are already equipped with RGAs. One reason is that the RGAs on tokamaks are rarely configured for real time measurements during tokamak discharges. A second reason is mass-resolved analysis does not permit distinguishing helium from molecular deuterium, since both particles have a mass of 4 AMU.

Reproducible operation of a commercial Penning gauge near a tokamak is only possible with magnetic shielding of the gauge assembly against the time-varying fields of

the tokamak coil systems. A magnetic shield box sufficiently thick not to saturate is mechanically secured against the magnetic forces on it --- force considerations usually dictate placement of the gauge a meter or more distant from the vessel port. Vacuum conductance between the vessel port and the gauge determines the time response. If most of the conductance comes from tubulation behind a torus isolation valve, differential pumping behind the valve may be employed to lower the pressure into the molecular flow regime and thereby shorten the response time.

Strong, spectrally-isolated emission lines exist for the neutral atoms of helium (He), neon (Ne) and argon (Ar). Consequently, photomultipliers equipped with narrow bandpass interference filters provide adequate spectral discrimination to monitor their intensities. On DIII-D, He, Ne and Ar are monitored with 1nm-wide bandpass filters centered on the 587.5, 640.1 and 811.5 lines, respectively. The pressure range for this system extends from 10^{-5} torr to 1.5 10^{-2} torr deuterium pressure. Within this pressure range, helium concentrations from 0.5-20%, neon concentrations from 0.5-10%, and argon concentrations from 0.2-1% can be routinely measured.

The partial pressure of each gas constituent can not be derived directly from its individual optical signal, due to optical crosstalk between the atomic lines of the noble gases and the comb-like, band spectra of molecular hydrogen. Consequently, the deuterium D_a line is measured simultaneously with the noble gas lines as a monitor of the deuterium pressure and the intensity of the interfering D_2 molecular lines. The partial pressures of the noble gases are then derived from the combination of their measured line intensities and that of D_2 using algorithms determined by calibration against an absolute pressure manometer.

So long as the spectral line monitored falls in the visible or IR, fiberoptic coupling may be utilized to place the optical detection system outside the tokamak Machine Hall, where it is less subject to electrical and neutron-induced noise.

Monitoring tritium concentration by optical detection of its lines in a Penning gauge requires more sophisticated hardware than is the case for the noble gases described above. The small spectral separation in the emission lines of the three hydrogen isotopes H, D and T necessitates use of a high-resolution spectrometer to separate the contributions of one from another[41].

C. Partial pressure measurements with an RGA

Characterization of component partial pressures in the residual gas of ultrahigh vacuum systems has been considered essential since pressures of $<10^{-8}$ torr were achieved and successfully measured in the late 1940's. Development of a residual gas analyzer (RGA) for measurement of component partial pressures began with the Omegatron in 1949, time of flight spectrometers, the radio frequency linear mass spectrometer, and the cycloidal spectrometer and Farvitron[42], each with limitations on resolution, mass range, and other disadvantages such as size and magnetic field requirements. The quadrupole mass spectrometer (QMS) was originally developed by Paul and Raether in 1955[43] and is now the most dominant technology in use for partial pressure analysis of gaseous systems.

The QMS detector is made up of an ion source, an analyzing region, and a detector. Ions formed at the source are injected through a collimating aperture into the centre of the analyzing region made up of four rods. The rods are electrically biased using a constant DC potential, and a variable rf potential. Ions initially traveling parallel to the rods come under the influence of the electric field. For a given rf potential, $V\cos(\omega t)$, one resonant

mass value will exist such that $m = 5.65\left(Vq/r_o^2\omega^2\right)$ for ion charge q and rod radius r_o. All other ion masses will oscillate with increasing amplitude, eventually striking a rod and neutralizing. Those ions that reach the opposite end of the analyzing region are counted in a detector made of either a Faraday cup, with a minimum detectable partial pressure between 10^{-10} and 10^{-13} Torr, or electron multiplier with pressures down to 10^{-15} Torr.

This type of RGA system is cost effective, has a detection level of parts per billion, is compact in size and weight (i.e. handheld), has a wide mass detection range commonly up to 300 AMU, and a fast scan speed per acquired mass of as low as 10 ms/AMU. Typical applications for QMS RGAs included monitoring global leak rate and distinguishing potential leak sources (internal or external) based on the measured mass spectrum (water, purge gas, air constituents (nitrogen, oxygen, argon), etc. For molecules, the mass spectrum is compared with that of known cracking patterns in order to determine its original composition (e.g. when bombarded with electrons, CO_2 produces a characteristic mass spectrum with peaks at mass numbers 28 indicating CO^+, 12 for C^+, 16 for O^+ and 14 for CO^{++}).

Additionally, QMS devices are now available in both a traditional open ion source (OIS), and closed ion source (CIS) configurations. In an OIS RGA, the entire ion source, typically an anode grid, quadrupole mass filter and detector operates at the pressure of the vacuum system, limiting operation to pressures below 10^{-4} Torr and reducing the ionizer sensitivity at higher pressures due to background interference. A CIS RGA remedies this by utilizing a tubular anode connected to the vacuum chamber where electrons, produced by a nearby filament, enter and ionize the gas. Ions then pass into the quadrupole mass filter in a separately pumped tee through a small aperture. In this arrangement, much higher chamber pressures may be sampled, up to 10^{-2} Torr, allowing the RGA to be used for online monitoring of gaseous processes.

Absolute confidence in QMS for quantification of gaseous species is limited, depending on calibration frequency, drift in detector linearity, cross species sensitivity, and detector stability. At best, after correct calibration, a QMS-based RGA is accurate to a few percent[44,45]. In tokamaks, RGAs are used extensively for leak detection and qualification of vacuum quality necessary for high performance plasma operation. A QMS-based system is ideal for co-existence with a tokamak as it requires no magnetic fields, and their components can typically be baked at 200-300°C for extended periods of time. RGA systems are typically used in the primary vacuum vessel, neutral injection beamlines, and other large vacuum systems connected to the torus.

On DIII-D, a traditional OIS RGA is used for this purpose[46,47]. Data is not typically taken during plasma operation due to the relatively short shot duration of 5-10 seconds. A CIS RGA is added for use during helium glow discharge cleaning (HeGDC), which is performed to desorb hydrogen and impurities from the walls, thus reducing recycling, easing plasma density control especially at low $\overline{n_e}$ and in low q operation, and reducing time required for post-disruption recovery. This is done for 5-10 minutes before all plasma shots, at pressures of 1-4 mtorr He in the vessel.

Recently at DIII-D, RGA spectra taken during HeGDC were analyzed in order to quantify escape of an isotopically enriched tracer gas[48]. Here, $^{13}CH_4$ was injected from a toroidally symmetric plenum at the top of the machine and entrained in a plasma flow, ultimately being deposited primarily on the inner centerpost and lower, inner divertor of the machine. Calibration of the RGA with a $^{12}CH_4$ small orifice leak was carried out immediately afterwards, and used to quantify escape of ^{13}CH-containing hydrocarbon molecules (e.g. $^{13}CH_4$ at mass 17).

Operation of RGAs for neutral particle characterization at the edge of the SOL or in the private flux region has also been carried out at tokamaks during plasma operation. On

Alcator C-Mod, argon impurity density has been monitored using an RGA sampling a limited mass range in order to determine impurity compression and enrichment ratios under reactor-like conditions[49]. Due to its long-pulse capability, the superconducting HT-7 tokamak has employed RGA data to infer hydrogen retention in the wall and its release during plasma operation[50].

For ITER[51] and DEMO-scale reactors, RGAs will necessarily include components – most notably the quadrupole head – that are in close proximity to the vacuum vessel to allow sufficient conductance between them. These will be subject to a significant ionizing radiation field, which is severely detrimental to electronics typically associated with RGA control. In anticipation of D-T operation at JET, this problem was overcome by development of an RGA using vacuum tubes and radiation hardened electronics at the quadrupole head adjacent to the torus, and isolating the control electronics in a diagnostic hall ~ 100 m away[52]. These modifications were made without significant loss to the dependability, sensitivity or resolution of the detector.

IV. PROBE MEASUREMENTS

Introduction

In recent years, a growing awareness that the plasma edge is determinant for the establishment of high confinement regimes (H mode, VH mode, etc.)[53,54,55,56], is driving a significant amount of research and diagnostic development for the edge, since it is generally believed that the origin of anomalous edge particle transport in tokamaks is electrostatic turbulence-driven transport[56,57,58,59]. Additionally, characterizing the plasma edge and scrape-off layer (SOL) of fusion devices is important to gauge discharge performance, understand the properties of the edge and SOL plasmas[60], evaluate their interaction with the plasma facing components and to understand some of the basic physics issues such as turbulence and anomalous radial particle transport. Understanding the tokamak boundary has profound implications for large fusion projects such as ITER and future fusion devices since their performance is limited by the heat load on the plasma-facing wall. The future fusion needs are therefore driving an effort in plasma modeling[61,62,63,64,65] which requires a large database of high spatial resolution edge/SOL data for validation and scaling purposes. Langmuir probes can provide the required data with 1-2 mm spatial resolution needed for the usual profile decay lengths (10-20 mm) in the edge/SOL of fusion devices.

Langmuir probes are successfully used in many plasma devices[66,67,68,69,70] such as plasma reactors, linear machines and fusion experiments, providing measurements of electron temperature, density and other parameters. In fusion devices, such as tokamaks, turbulence is found to be responsible for a considerable part of the energy and particle losses in the boundary plasma[71,72,73,74,75,76]. Turbulent particle transport studies are routinely performed using multi-pin probe configurations[76,77,78] and the different pins are

used for simultaneous measurements of fluctuating floating potential $\tilde{\phi}_f$, poloidal and radial electric fields $\tilde{E}_\theta, \tilde{E}_r$, the local plasma density n and its fluctuations $\tilde{n}$. The evaluation of turbulence-driven radial particle transport $\tilde{\Gamma}_r$ is possible by cross-correlating the fluctuating quantities. Electron temperature fluctuations $\tilde{T}_e$ enter the particle flux calculations through the electric field inferred from the difference of floating potentials at spaced probe pins[79] and from the evaluation of density fluctuations from saturation current fluctuations.

$$\Gamma_r = \frac{\langle \tilde{n}\, \tilde{E}_\theta \rangle}{B_\phi} \tilde{E}_\theta = -\nabla_\theta \tilde{\phi}_s = -\nabla_\theta (\tilde{\phi}_f + 3.5 k \tilde{T}_e) \frac{\tilde{n}}{\langle n \rangle} = \frac{\tilde{I}_{sat}}{\langle I_{sat} \rangle} - \frac{1}{2} \frac{\tilde{T}_e}{\langle T_e \rangle} \tag{1}$$

The contribution of $\tilde{T}_e$ on such calculations is often neglected under the assumption, based on limited experimental results[77,79], that $\tilde{T}_e / T_e \leq 15\%$ in the edge and that the phase between $\tilde{E}_\theta$ and $\tilde{T}_e$ is π, corresponding to a strong correlation. However, reports[77,80,81,82] of higher levels of temperature fluctuations may bring a certain part of conventional evaluation of particle transport under question. The cross-field heat transport can be expressed as the sum of convective and conductive terms:

$$\tilde{Q}_{tot} = \tilde{Q}_{cond} + \tilde{Q}_{conv} = \frac{5}{2} \frac{\langle \tilde{T}_e \tilde{E}_\theta \rangle}{B_\phi} + \frac{5}{2} \Gamma_r T_e \tag{2}$$

A requirement of these measurements, which may not be met by all diagnostic systems, is that all the fluctuating quantities are measured within a correlation length (poloidal, radial and toroidal) i.e. that the plasma sampled by the various tips is the same. Many probe diagnostic techniques used so far[79,80] do not necessarily meet the requirements of locality, especially in turbulent conditions. Among the techniques used for these measurements is the triple probe technique[83]. This technique, which is otherwise straightforward, is challenged by the need to sample a small plasma volume with three tips and maintain very accurate tip geometry, especially for high time resolution

measurements of turbulent plasmas. The fast-sweep single probe technique can be difficult because the probe characteristics are affected by fluctuating electric fields, resulting in apparent temperature fluctuations. This requires high sampling rates and multi-parameter fitting, and can require high supply currents and voltages.

Operation of Langmuir probes is based on the non-linearity of the single Langmuir probe characteristic. The current to the single tip, assuming Maxwellian populations[84] can be written as:

$$I_{pr} = I^{+} - I^{-}\exp\left\{e(V_{pr} - V_s)/kT_e\right\} \tag{3}$$

Where $I^{+} = 0.5en_eSc_s$ is the ion saturation current, $I_e^{-} = -0.25en_eSc_e\exp(\psi)$ is the electron current, $I^{-} = -0.25en_eSc_e$ is the electron saturation current, $c_s = [k(T_e + Z\gamma_i T_i)/m_i]^{1/2}$ is the sound speed, $c_e = [8kT_e/m_i]^{1/2}$ is the thermal electron velocity, S is the effective collecting area, ψ is eV/kT_e, V_s is the plasma potential, V_{pr} is the probe potential, m_i is the ion mass, T_i and T_e are the ion and electron temperature, Z is the charge state and γ_i is the ion adiabatic constant. Often, $T_i = T_e$, $Z = 1$ and $\gamma_1 = 1.5$ are assumed.

The equation above can be solved for the potential when $I = 0$, or so-called floating potential, obtaining:

$$V_{fl} = (kT_e/e)(1/2)\ln(m_i/2\pi m_e) \tag{4}$$

Thus Eq. 1 can be rewritten as:

$$I = I_{sat}^{+}\left\{1 - \exp\left[e(V_{pr} - V_{fl})/kT_e\right]\right\} \tag{5}$$

Single probe

Application of probes to measure plasma parameters can be seen by a cursory look at Eq. (3) that indicates that if a probe tip is immersed in a plasma and a sweeping voltage is

applied to it, the collected current will vary as shown in Fig. 3. Thus, by measuring the applied voltage and the resulting current, the remaining free parameters (under the simplifying assumptions described above) are the plasma density (Ne) and temperature (Te). A single probe schematic setup is shown in Fig. 4, and it is customary to use a sweeping voltage to the probe tip and use multi-parameter fits (Te, Ne and even Vfl) to the I-V characteristic to obtain the desired measurements.

The frequency and amplitude of the sweep varies considerably depending on the application although it is common to keep the sweep frequency about 1 kHz (for usual reciprocating probe speeds yields 1 data point per 1-2 mm) and to sweep the voltage between ion saturation current and the floating potential to avoid the electron saturation branch and reduce current requirements.

An example of current-voltage measurement, Fig. 5 shows NSTX data obtained via an optically isolated voltage amplifier (to isolate from plasma high voltage) and an inductive current sensor (in this case a Pearson transformer) to also provide isolation. An alternative scheme for current measurement can be implemented with a shunt resistor and an optically isolated amplifier.

Double probe

Although the single probe technique is quite powerful, ion saturation must be reached for a proper fit and that can require quite high voltages ($\sim$ 3kTe below floating potential to reach ion saturation) if the plasma potential is large with respect to the reference ground. A way to circumvent this issue is to use two tips connected to each other via a power supply (see Fig. 6) and floating with respect to any ground so that the plasma itself is the reference and therefore a voltage swing of only $\sim$ 3kTe is needed to reach saturation independent of the plasma potential.

An equation for the double probe can be easily inferred from that for a single probe by observing that the current is conserved in the closed loop formed by the power supply and plasma.

$$I = I_{sat}^{+}\left\{1-\exp\left[e(V_1 - V_{fl})/kT_e\right]\right\} = -I_{sat}^{+}\left\{1-\exp\left[e(V_2 - V_{fl})/kT_e\right]\right\} \quad (6)$$

Where V_1 and V_2 are the potentials applied to tips 1 and 2 respectively. Considering that $V_{Bias} = V_2 - V_1$, it can be rewritten as:

$$I = I_{sat}^{+}\tanh\left(eV_{Bias}/kT_e\right) \quad (7)$$

Thus the current-voltage characteristic for the double probe can be fitted using a three free parameter curve once collected current and voltage are measured and the usual simplifying assumptions are made. Typical double probe data from NSTX is shown in Fig. 7.

Harmonics Technique

The arrangements mentioned above measure N_e and T_e by sweeping the probe voltage and require entering ion saturation current. The harmonics technique, a variation of the single probe technique, does not require entering saturation current and is therefore advantageous in very dense, hot plasmas since the collected current and required voltage are dramatically reduced. This technique is ideal for fast Te measurements and has been long known[85,86] although under somewhat restricted application space; and its use in a tokamak plasma was recently implemented[87] in TEXTOR, albeit in a low bandwidth version. Subsequent measurements with higher temporal resolution $(10\ \mu s)$ were performed in the small tokamak TF-1 IVTAN (USSR),[88] and the first evaluation of the technique for $\tilde{T}_e$ measurements was performed in TEXTOR[89].

The setup described here is floating (a capacitor is in series with the tip) so we can

write $V_{pr} - V_o = U_o \sin \omega t$ when an oscillating potential of amplitude U_o and frequency ω is applied to the floating probe. The operating potential of the tip V_o, is different from the floating potential V_f as it will be shown later. The periodic exponential term can be written[90] in terms of Bessel functions $I_k(z)$ of integer order k:

$$e^{z\cos(\theta)} = I_o(z) + 2\sum_{k=1}^{\infty} I_k(z)\cos(k\theta) \tag{8}$$

The probe current density can be written as:

$$I_{pr} = en_e c_s - \tfrac{1}{4} en_e c_e \left[e^{eU_o \sin(\omega t)/kT_e} \; e^{e(V_o - V_s)/kT_e} \right]$$

$$= en_e c_s - \tfrac{1}{4} en_e c_e \left\{ e^{e(V_o - V_s)/kT_e} \left[I_o(\tfrac{U_o}{kT_e}) + \sum_{m=1}^{\infty} I_m(\tfrac{U_o}{kT_e})\cos(m\omega t) \right] \right\} \tag{9}$$

Note that the expansion of the exponential produces a DC (non-oscillating) current term that has to be accounted for when the floating condition $I_{pr}^{DC} = 0$ is implemented in order to solve for the operating potential V_o. The operating potential is that at which the ***total*** DC current (including the AC-generated current or rectification current) to the probe is zero. Thus:

$$I_{pr}^{DC} = en_e c_s - \tfrac{1}{4} en_e c_e \left\{ e^{e(V_o - V_s)/kT_e} \left[I_o(\tfrac{U_o}{kT_e}) \right] \right\} = 0 \tag{10}$$

We can calculate the operating potential as:

$$eV_o = eV_s + kT_e \ln\left[\frac{4c_s}{c_e} \frac{1}{I_o(\frac{U_o}{kT_e})} \right] = eV_s + kT_e \left\{ \ln\left[\frac{4c_s}{c_e} \right] - \ln\left(I_o(\tfrac{U_o}{kT_e}) \right) \right\} = eV_f - kT_e \ln\left(I_o(\tfrac{U_o}{kT_e}) \right) \tag{11}$$

The last term on the right-hand side is written in terms of the standard floating potential V_f and it is clear that the net effect of the new term is to shift the operating voltage of the probe to a value below V_f. This effect is a self-bias caused by an oscillating potential in

the plasma or probe and is well known in the rf plasma-processing community. The probe characteristic is thus modified to:

$$\left\{\frac{2}{I_o(\frac{U_o}{kT_e})}\sum_{m=1}^{\infty} I_m(\frac{U_o}{kT_e})\cos(m\omega t)\right\} = 2\sum_{m=1}^{\infty} I_{m\omega}\cos(m\omega t);\ I_{m\omega} = I^+\frac{I_m(\frac{eU_o}{kT_e})}{I_o(\frac{eU_o}{kT_e})} \tag{12}$$

It should be noted that previous work in this subject[86,87,88] ignored the DC term due to the oscillating potential. The Bessel functions, $I_m\left(eU_o/T_e\right)$ have an argument depending solely on the amplitude of the applied voltage and the electron temperature. The creation of multiple harmonics $m\omega$ when the probe is excited by a frequency ω is then understood as caused by the nonlinearity of the probe characteristic. The evaluation of T_e is possible from the ratio of any two harmonics of the probe current. The ratio of two harmonics $I_{m1\omega}$, $I_{m2\omega}$ is independent of the zero-order Bessel function correction. In particular, the ratio $I_{2\omega}/I_\omega$ features higher sensitivity than that of other low harmonics for a given eU_o/kT_e, and therefore such ratio is preferred:

$$\frac{I_{2\omega}}{I_\omega} = \frac{2I^+}{2I^+}\frac{I_2}{I_1} = f(U_o/kT_e) \tag{13}$$

The ratio of the first two harmonics is fairly linear with eU_o/kT_e up to $eU_o/kT_e = 1-2$, and rolls over above that value, implying loss of sensitivity. It must be noted that large values of eU_o/kT_e can not treated properly by Eq. 1 because it does not include the electron saturation branch which occurs when $eU_o/kT_e \sim 3.5$ although in reality, Eq. 1 is probably inaccurate before then. Furthermore, experimental work[91] has shown that the description embodied in Eq. 1 breaks down for $V_{pr} \geq V_f + kT_e$ roughly corresponding to $eU_o/kT_e \geq 1$ and heretofore considered a practical (albeit somewhat arbitrary) limit for the harmonic technique. To evaluate T_e in practice, the amplitudes of the first two current harmonics I_ω and $I_{2\omega}$ are separated by digital filtering, their ratio calculated and the value of eU_o/kT_e corresponding to that ratio is obtained by inversion

of Eq. (7) which can be simplified by using tabulated values and interpolation or a linear expansion valid for $eU_o/kT_e < 1$ since the Bessel functions can be expressed in a series expansion given by[90]:

$$I_k(z) = \sum_{n=0}^{\infty} \frac{z^{2n+k}}{2^{2n+k}(n+k)!\,n!} \tag{14}$$

An analytical expression for the amplitude of the first three harmonics can be obtained by taking the first term of the expansion with the condition $eU_o/kT_e < 1$:

$$I_1(eU_o/kT_e) = \frac{eU_o}{2kT_e},\ I_2(eU_o/kT_e) = \frac{1}{8}\left(\frac{eU_o}{kT_e}\right)^2, \text{ and } I_3(eU_o/kT_e) = \frac{1}{48}\left(\frac{eU_o}{kT_e}\right)^3 \tag{15}$$

If we use the ratio of the first two harmonics, the temperature can be expressed as:

$$kT_e \approx \frac{eU_o}{4}\frac{I_1}{I_2} \tag{16}$$

When $eU_o/kT_e = 1/2$ the error over the exact calculation is about 1 %, increasing to 5% when $eU_o = kT_e$ and diverging rapidly thereafter.

Probe Drive Systems

As mentioned above, an important challenge for probes in fusion plasmas is to reduce heat and particle fluxes to the probe components to prevent probe damage and plasma contamination while performing the measurements. The solution to the problem has been the emergence of the fast reciprocating (or scanning) probe systems. Original fast scanning probe designs were all metal construction and therefore not suitable for today's high performance machines, where the high plasma temperature and density would erode the metal tips and contaminate the plasma with high Z materials. New probe systems have been recently developed[92,93,94] for the newer, high -performance fusion devices, and are designed specifically to reduce plasma contamination, resist high heat and particle

flux and withstand forces induced by disruptions. The new probes tend to be more complex and difficult to maintain.

Although there are quite a few probe drive systems in operation in the world, they share most characteristics. The system described here, installed at NSTX shares common design features, such as modular head and tip design for ease of replacement, industry standard modular control system, high-speed operation, high heat flux capability, and high bandwidth operation to 5 MHz for turbulence measurements. The system also implements some new solutions such as replaceable and rotatable shaft and circuit board interconnects to replace bulky cables. We will also describe how they meet the stringent requirements imposed by the modern[95] plasmas and facilities.

Probe Description

Most modern probes are based on a reciprocating system located near the midplane in the low field side of tokamak, as seen in Fig. 8. Some installations have probes at a different poloidal location, such as the X-point and located horizontal or vertical.

Most probe assemblies consist of two main parts: The drive mechanism and the probe itself, both mounted on some sort of backbone that rests on a support structure. The probe system interfaces to the tokamak via a bellows to accommodate thermal expansion and shifts and a gate valve to isolate the torus from the probe during maintenance. Many systems are pumped separately from the main torus.

Design requirements

The main criteria for the probe design are given by three, often contradictory, mandates, namely: 1) The need to obtain high spatial and time resolution measurements that provide input to simulation codes, often needing as deep a plasma penetration as possible, 2) survive the plasma-generated heat and particle fluxes that destroy the probe

materials or induce arcing and can contaminate the plasma and, 3) allow remote operation in the often-inaccessible environment of a tokamak. We will present them in some detail.

-Ability to obtain the needed measurements.

- Electron temperature $T_e(r)$ and density $n_e(r)$ profiles with 1-2 mm spatial resolution (less than the 10-15 mm profile decay length). Needed by simulation codes to define SOL and pedestal profiles.

- Poloidal electric field $E_o(r)$ and radial electric $E_r(r)$ profiles needed to define radial and poloidal drifts.

- Profiles of fluctuation levels in density n_e, poloidal and radial electric fields, $E_o(r)$, $E_r(r)$, and electron temperature T_e, with bandwidth of up to 3-5MHz and spatial resolution of 1-2 mm. Needed to evaluate turbulent components of particle and heat transport and other effects such as Reynolds Stress.

-Survive the plasma generated heat and particle fluxes.

The probe shaft, head and tips should:

- Withstand a heat flux of 10 MW/cm^2 while keeping the graphite head and tips temperature below 1600 deg C.

- Withstand particle fluxes of the order of 10^{19} cm^{-2} s^{-1} without losing structural integrity between maintenance events (usually a few months).

- Be compatible with a base pressure of 1x10^{-8} Torr

- Bakeable to 150 deg C.

- Hold a potential of 3-5kV to ground.

- Be made of low Z materials so as not to contaminate the plasma.
- Withstand forces generated by accelerations of up to ~ 100 g's.

-Ease of maintenance and simplicity of operation.

Due to the harsh conditions to which the probe is exposed, progressive damage to the tips and head occurs during normal use. Thus a system to ease the replacement of those is mandatory in these probes. Additionally, access to diagnostics in tokamaks is usually impaired during operation due to radiation, high voltage environment, and space and time constrains. The reciprocating system should, therefore be as reliable and simple as possible in order to reduce downtime and ease repairs.

Probe

The probe system assembly is comprised of two main parts, the probe itself and the drive mechanism. The probe is composed of the head, shaft and feedthrough and should be as light as possible in order to increase acceleration (and ultimate speed) and decrease the forces generated during operation. The head is exposed to the plasma for a brief time $(\sim 100 \text{ ms})$ on every plunge and should therefore be easily replaced or maintained.

Probe Head

A very capable probe head would have about twelve tips and such is the system described in detail here[96]. The tips need to be made of a material with high heat conductivity to remove the impinging heat flux. The ones described here are made out of Thermalgraph CFC (with parallel thermal conductivity of 900 W/mK, twice as much as copper) and mounted on a Boron Nitride (BN) matrix for electrical insulation, as shown in Fig. 9. The whole structure is protected against high heat fluxes by a graphite shroud, shown in Fig. 10, yet a small section of BN is exposed as also shown on Fig. 10 and

Fig. 11 (detail) in order to prevent the graphite (a conductor) from setting boundary conditions for the electric fields. The exposed dimensions of the tips are 1.6 mm length *l* and 1.5 mm diameter *d*. The tips are filed to a tolerance of 0.1 mm in length by using a filing jig. The probe needs to conform to the flux surfaces which in this case have significant poloidal curvature and move away in the poloidal direction. Therefore, the probe face and tips need to follow that contour. In the case of NSTX this requires on average an angle of 11 degrees, as shown in Fig. 9-a.

The probe tips are aligned in the toroidal direction as seen in Fig. 9-b, in such a manner that magnetic field angles between 25 and 45 degrees are possible without mutual tip shadowing yet allowing them to sample approximately the same plasma. The standard NSTX magnetic field pitch angle is approximately 35 degrees at the edge, and it is closer to 3-4 degrees in conventional tokamaks. As an example of probe use, two tips (Double-1, Double-2 in Fig. 9-b) are used as a double probe pair. One tip is at ion saturation (I_{sat}), three poloidally separated tips $\left(V_{f1}, V_{f2}, V_{f5}\right)$ are floating to measure the floating potential (and, by substraction, the poloidal electric field) and tips V_{f3}, V_{f4} are also floating and displaced 1.6 mm radially from V_{f2} to measure the radial electric field. The floating tips have a 100 KOhm vacuum resistor (much higher than the plasma sheath impedance) in series to ground.

The constant wear on the head and tips make it mandatory to periodically replace the tips and occasionally, the BN insulator and graphite shield. Exposure to carbon released from various plasma-facing components will slowly coat the BN insulating piece and will short the tips electrically, so its replacement or cleaning has to be foreseen. Given the limitations stated above, the head has been designed in such a way that parts replacement is a fast and simple operation.

The approach taken in this design is shown on Fig. 10 and it consists of 6 removable

BN sections which provide electrical insulation, thermal conduction and mechanical strength. The first one is fixed to the shaft and features pin connectors, the second one is a buffer piece which holds the connections to the circuit board, the third one encases the circuit board itself, the fourth one consists of a board-tip interface and the fifth and sixth ones hold the tips in place. The sixth one is partially exposed to the plasma, as shown in Fig. 9-a. All the BN pieces are notched as shown on Fig. 10 in order to prevent rotation during assembly and operation. The tips are threaded in the back to accept a short piece of Inconel rod that crimps to the wires leading to the PC board. The head assembly is held in place by long screws (Fig. 10) and the graphite shield, which is in turn screwed onto the Inconel shaft. The whole head assembly is attached to the shaft via a threaded connector, which makes the whole head readily replaceable.

Shaft

The probe shaft, seen in Fig. 11, is made out of Inconel tubing, which features the head assembly at the front end and houses a set of semi-rigid coaxial vacuum cables. The coaxial cables act as transmission lines (50 Ω load), assuring good frequency response. The cables connect the tip assembly to a 21 custom feedthrough system which is fastened to the rear of the probe shaft as show in Fig 11. The coaxial cables are Vespel-isolated to keep vacuum compatibility and breakdown voltage requirements. The cable insulation is built out of Polyimide (Vespel trademark by Dupont), which is an easy to machine material, lightweight and strong (85-95 Rockwell H), resists high temperatures (300 deg. C) and has a very low outgassing rate[97] ($4x10^{-10}$ Torr-l /sec-cm^2 at room temperature and $3x10^{-6}$ at 300 deg C). Vespel is slightly hygroscopic and absorbs water upon air exposure, which is then released during bakeout; therefore Vespel is used within a highly vented probe shaft to allow pumping.

Circuit Board

An innovative element of this probe design is the use of high vacuum, high temperature printed circuit boards (PC boards) to reduce the complexity of cabling in small spaces and also to accommodate complex sensors. Although the use of PC boards is presently limited to the probe head, it is planned to extend to the shaft as well. The board material has to be compatible with vacuum (low outgas rates), and resist baking temperatures to 150 deg. C. The material chosen is Pyralux FR-9120. The advantage of a circuit board is three-fold:

-Provides an ultra-compact platform to install sensors and other components.

-Reduces the weigh of the probe head

-Reduces the complexity in design and assembly of the head. Particularly when sensors are added.

The PC board used in the probe head is shown in Fig. 12. It has been folded in a channel shape to decrease its dimensions and increase its rigidity. The components shown, such as the 100 kOhm resistors, are surface-mounted and therefore extremely compact.

Probe Drive

The probe drive mechanism should be made as fast as possible in order to limit the time of exposure of the probe head and tips to the plasma. Its design is therefore, a compromise between the desire to obtain enough statistics on the data and reducing damage to the probe at a reasonable cost. We have developed a distinctive, two-stage design drive using as many off-the-shelf parts as possible to reduce costs.

The drive mechanism is based on the philosophy that the probe should move powered by a slow step motor and worm screw drive to a stand-by position where it is close to the plasma, but not exposed to it, and then should reciprocate from there rapidly, powered by a fast pneumatic cylinder when triggered by the control system. Therefore, the probe assembly consists of a fast plunge section, which is carried on top of a slow plunge section, as shown in Fig. 13. The pneumatic drive is rugged, dependable, and accurate, with position reproducibility to within $< 1\%$.

The slow plunge section consists of a carriage table fastened to bearing sliders, as shown in Fig. 13, which move on a linear track fastened to the probe backbone. This section is powered by a stepper motor, moving a worm screw. The position of the carriage, measured by a digital encoder, is thus adjustable and can be varied by 30 in. (76.2 cm), determining the deepest penetration of the probe (since the fast plunge throw is a constant 8 in. or 20.32 cm). The worm screw is equipped with an electromechanical brake for safety. The digital counter interfaces with the control system and its readout position is continually compared to the final desired position. Two compressed air-powered pistons are located on the sides of the carriage (not shown for clarity) and in the case of a vacuum accident, a relatively fast retrieval of the probe (1 s) behind a gate valve is possible.

Once the slow plunge section is placed in position, the fast plunge section, moved pneumatically by a cylinder powered by helium at 40 PSI, reciprocates when the fast valves are triggered by the control system. This type of cylinder has multiple valves controlling the inlet and outlet ports and thus offers a variable dwell penetration or detailed timing for the probe that can be fully programmed from the control system.

The position of the probe as a function of time is digitized from a potentiometer at 1 MHz and shown in Fig. 14a. The velocity and acceleration are calculated from the

position. The time intervals of interest are labeled from 1 to 5. The speed and acceleration are shown in Fig 14b and 14c respectively. At time 1, shortly after the beginning of the plunge, the acceleration has a local maximum $(\sim 100$ g's$)$, causing the probe to reach its maximum speed of 2.5 m/sec at interval 2. Briefly thereafter, the acceleration increases to ~ 150 g's as the helium backpressure starts to bring the probe to a halt (interval 3). The probe stops for a very brief interval, still under heavy acceleration, and starts moving back in interval 4 at a slightly reduced speed due to lower forces as the helium pressure drops. It is finally brought to a halt by a surge of pressure in interval 5. It is important to mention that the substantially higher speed of sound in helium offers improved performance over air and that the use of a gas reservoir to maintain the helium pressure during operation is crucial.

Control System

The probe system is fully controlled by a commercial PLC that receives all the input signals from the various probe sensors (limit switches, rotary encoder) and the NSTX Interlock System to determine the probe and facility status. These inputs are combined with a set of rules to maintain facility and personnel safety while protecting the probe.

The operators interact with the PLC (i.e. the probe system) via terminals that communicate with the PLC over optical fibers. One terminal is located in the control room and the other in the NSTX test cell, so operators can fully control the probe at either location.

Measurements in NSTX

The probe is located slightly below (8" or 20.32 cm) the outer midplane of the machine, where the toroidal magnetic field B_T is roughly 2.3 kG during standard operation and therefore the size of the ion and electron gyroradius are $\rho_e \sim 5 \times 10^{-3}$ cm,

$\rho_i \sim 0.25$ cm for a range of electron T_e and ion T_i temperatures encountered in the NSTX edge (we assume $Ti \sim Te$, $\sim Te \sim 50-200$ eV) which means we operate in the magnetized regime for the electrons but not for the ions since the probe tip dimensions are 1.6 mm in length and 1.5 mm in diameter[60] and should use the full area A_p of the probe tips as the collection area[98], i.e.

$$A_c = A_p = l \times \pi \times d \text{ or } \sim 7.5 \text{ mm}^2. \quad (17)$$

The probe tips, of length l and diameter d, collect plasma from -and therefore average over- a certain length along the magnetic field called collection tube. The toroidal extent L_p of this perturbation can be estimated[53] if we know the ion perpendicular diffusion coefficient $D_\perp$ and the sound speed c_s by:

$$L_p \approx (dlc_s)/(8D_\perp) \quad (18)$$

For the values of T_e and T_i given above and using $D_\perp = 0.6-1 \sim \text{m}^2/s$ we obtain[99] $L_p \approx 30$ mm. Therefore the data is averaged over ~ 3.0 cm in the toroidal direction, averaging that does not affect our results since the parallel gradients in most tokamaks are only appreciable in the vicinity of significant sinks or sources of particles and energy such as those present near limiter and divertor plates.

The probe also measures radial profiles of the floating potential Vf(t) at five locations, three separated poloidally and two radially, and therefore we can calculate poloidal, $E_o(t)$, and radial, E_r, electric fields. The saturation current $I_{sat}(t)$, and double probe characteristics every 1 ms are obtained as well. We measure fluctuations at a digitization rate of 1 or 2 MHz (default is 1 MHz, which is shown to be adequate below). Anti-aliasing filters are used at either 500 kHz or 1 MHz, depending on the sampling frequency.

The double probe is swept with a 1 kHz sawtooth voltage of amplitude +-160V (i.e.

320 V peak-peak) as shown in Fig. 15 in order to provide a full current-voltage (I-V) characteristic every 1 ms. This provides values of the plasma electron density n_e and temperature T_e by fitting Eq. 4 to the data. We assume $T_i \approx T_e$, which is not true in general in the edge plasma, but is a good operating assumption since the current is a weak function of the temperature. The fit is done with 4 variables because offsets in the voltage and current are allowed, but convergence is usually straightforward. The signal to noise ratio (S/N) limit varies depending on plasma conditions, but reliable profiles are obtained up to 6 cm into the SOL, where the low I_{sat} causes loss of sensitivity to the variation of T_e. Our codes provide options for averaging 2 or 3 sweeps in order to improve the S/N ratio in exchange for some loss in spatial resolution. The applied voltage must be of the order of $2\ \mathrm{k}T_e$ to assure obtaining current saturation but we find that we can get reliable temperatures up to $>>120$ eV since we fit a known, very non-linear function and therefore the routine is able to calculate an I_{sat} compatible with the partial data. These signals are digitized at 1 MHz to resolve enough points (~ 500) per sweep. It is interesting to note that the error of the fitting varies with the sweep rate. This is due to the fact that large density fluctuations (of the order of 50%) exist at the plasma edge and the power spectrum of these fluctuations peaks at fairly low frequencies (1-20 KHz) as shown in Fig. 16. It can, therefore be deleterious to sweep too fast since the fluctuations are not averaged over time and the data is more noisy. We have found that a good compromise between good spatial (temporal) resolution and better fits exists at about 1 kHz.

An additional issue is the presence of plasma intermittency, which consists of fast, bursty events with duration of $30-60\ \mu$s, as shown in Fig. 17, and worsens the S/N ratio and covergence issues. Intermittency has been observed in a variety of magnetic configurations[100], tokamaks[101,102] and also in NSTX[103]. The intermittency is the result of fast plasma filaments that convect particles and energy rapidly towards the chamber

walls.

The double probe has the advantage that it is insensitive to high local voltages since it is a floating system. The tip that measures I_{sat} is, on the other hand, a single probe and biased by a power supply referenced to limiter ground and therefore is liable to lose saturation if the plasma potential itself is highly negative.

The radial profiles of all the quantities of interest can be reconstructed from the time-position information. The spatial resolution will depend on the voltage sweep frequency (1 kHz) and the velocity of the probe, which is variable with radius. At its fastest (2.5 m/s), the probe moves about 1.25 mm during a double probe sweep (half a period), that is in 1/2 ms, therefore the spatial resolution of the double probe measurements is about 1.6 mm (or the tip length). Typical spatial resolution in the core plasma is also 1.6 mm because the probe moves slowly there, as seen in Fig. 14.

Profiles of SOL electron density for three NSTX discharges with different input power, in high (H) and low (L) confinement modes, are shown in Fig. 18. Edge profiles of T_e and n_e are needed as input for codes which model the edge and scrape-off layer (SOL)[63,104] of tokamak plasmas by solving a set of coupled non-linear fluid equations, a particle source form the core, a sink from the divertor, and a neutral source. The calculations of these codes are needed for deeper understanding of edge plasma issues, to evaluate the plasma interaction with the walls and to produce scalings, which will help the understanding and design of future machines.

We find that the profiles in the SOL of NSTX are best fitted by the functions:

$$n_e(r) = n_{e0} + n_e(Rs) \times \exp(-(r - Rs)/\lambda_n) \tag{19}$$

$$T_e(r) = T_{e0} + T_e(Rs) \times \exp(-(r - Rs)/\lambda_T) \tag{20}$$

Where R_s is the radius of the last closed flux surface, n_{e0}, T_{e0} are offsets and λ_n, λ_T

are the characteristic decay lengths. The fit values for some edge density profiles in NSTX are shown in Fig. 18. Notice that the decay length is longest for a L-mode discharge, at 3.25 cm, is markedly reduced in H-mode to 2.55 cm (same input power at 2 MW) and further reduced to 1.51 cm at the highest power H-mode discharge. Therefore, the SOL thickness seems to be inversely proportional to the input power in NSTX.

It is crucial to notice that there is an offset on both the density and temperature profiles which will make purely exponential profile fits yield the wrong decay lengths. Exponential profiles are expected for simple, sourceless SOL, so the physical origin of the offset is probably the fact that the SOL has a significant particle source in it due to anomalously large convective transport.

The probe can also provide simultaneous measurements of the fluctuating quantities $\tilde{E}_\theta$ and $\tilde{n}_\theta$ and from them infer turbulent particle and heat transport as described by Liewer[105] and Powers[106]. These measurements are necessary in order to understand and characterize the underlying cause of anomalous energy losses in tokamaks, and, at the moment, can be performed only by probes. The probe system supports a bandwidth of $> 3\ \text{MHz}$, although the turbulence features significant power only up to $\sim 200 - 250\ \text{kHz}$, as seen in Fig. 16, where the noise floor is reached at about 300 kHz. The turbulence-induced particle flux, $\tilde{\Gamma}_r$, can be written in terms of an ensemble average of the density fluctuation level $\tilde{n}_e$ and the velocity fluctuation level, $\tilde{V}_r$ (in the direction of the flux) as:

$$\tilde{\Gamma}_r = \left\langle \tilde{n}\tilde{V}_r \right\rangle \tag{21}$$

With the assumption $k\rho_i < 1$ the expression for the radial flux becomes:

$$\tilde{\Gamma}_r = \left\langle \tilde{n}\tilde{V}_r \right\rangle = \left\langle \frac{\tilde{n}_e \tilde{E}_\theta}{|B_\phi|} \right\rangle = \frac{\left\langle \tilde{n}_e^2 \right\rangle^{1/2} \left\langle \tilde{E}_\theta^2 \right\rangle^{1/2}}{B_\phi} \frac{\left\langle \tilde{n}_e \tilde{E}_\theta \right\rangle}{\left\langle \tilde{n}_e^2 \right\rangle^{1/2} \left\langle \tilde{E}_\theta^2 \right\rangle^{1/2}} \tag{22}$$

notice that the radial flux can be written in terms of the RMS fluctuation levels of the poloidal electric field and density, quantities easily obtained with the described probe pin distribution, as explained before.

V. THERMOCOUPLES FOR HEAT FLUX MEASUREMENT

Thermocouples in most plasma devices are used for slow long-term measurements and do not have the time response necessary for heat flux measurement during the pulse. Because of the small signal levels produced by thermocouples and the consequent difficulty in discriminating against background noise, in may cases they are not monitored during the plasma pulse There are a few cases in which divertor heat flux has been measured using thermocouples.

In JET, the thermocouple measurements of tile temperature before and after the plasma pulse were used to determine the average power deposited to a tile during the pulse. By scanning the divertor strike point in small steps across a tile boundary from one shot to the next, a spatially resolved heat flux profile measurement was developed[107].

In DIII-D, a thermocouple was installed at a shallow depth near the plasma facing surface and an isolation amplifier was used to relay the signal from the tokamak. The temperature as a function of time was measured during plasma pulses and used to calculate heat flux onto the surface[108].

Standard infrared thermography of the divertor structures is difficult in C-Mod, due to the lack of line-of-sight views of surfaces in the closed divertor geometry. A novel method for measuring heat fluxes to the surface of the divertor was therefore investigated[109] based on an adaptation of a commercially available thermocouple device[110]. The adapted design employs a coaxial-like geometry with a ceramic coated tungsten-rhenium ribbon embedded in a 6.35 mm diameter molybdenum rod. The end of the rod is aligned with the outer divertor tiles, exposing a 5 deg ‘ramped’ surface to incident magnetic field lines. A thermocouple junction (tungsten-rhenium/molybdenum)

is formed at the plasma-facing end of the rod as the ceramic insulation breaks down there (first by machining the end of the rod, then by plasma interaction). Using a one-dimensional, semi-infinite slab model, heat fluxes parallel to field lines in the range of 50-500 MW m^{-2} can be inferred from the surface temperature evolution. An array of 10 units was deployed on the outer divertor, at locations similar to outer divertor probes. Representative traces of surface temperature and parallel heat fluxes profiles at three times for a discharge with 3 MW of ICRF heating power are shown in Fig. 19.

VI. EROSION and DEPOSITION MEASUREMENTS

A. DiMES erosion and deposition measurement

The Divertor Materials Evaluation System (DiMES) program in DIII-D was developed for the study of plasma-wall interactions and with the capability of exposing material samples to plasma discharges in the lower divertor. The DiMES system[111] has provided measured erosion and redeposition data of surface materials for future tokamak devices like ITER. Net material erosion and redeposition of carbon, W and Be have been measured and results have been used to benchmark modeling codes.

DiMES Experiment

ATJ graphite samples with diameter of 4.8 cm and polished to 0.25 μm finish on the plasma side, some with depth marker of silicon implanted at ~ 300 nm below the surface using a 200 kV ion beam can be inserted to the lower divertor of DIII-D. Metal films 100 nm thick are deposited on the graphite surface via electron beam evaporation deposition, or solid lithium foils may be physically applied. After the desired plasma conditions have been obtained, the sample is inserted and exposed to selected single plasma conditions. This is critical in that the erosion results obtained are related to the particular discharge. We have exposed samples to various plasma regimes: high and low beam heating discharges, edge localized mode (ELMs) and disruptions. Several exposures were used to accumulate exposure time of 4–20 s. Description of the DiMES experiment, its operation in DIII-D, its experimental methods are presented in[112-116]. Erosion measurements are tied to well-characterized plasmas using the full set of divertor diagnostics. For the absolute measurement of net erosion, the Rutherford back scattering

(RBS) analysis is conducted using a beam of 2 MeV He+ to detect the effective depth of a pre-exposure implanted Silicon depth marker. Precision of the depth measurements is ±10 nm. Nuclear Reaction Analysis (NRA) is used to measure the amount of transported Be to the surrounding carbon surface. Retention of deuterium in the samples is mapped by NRA from the $d(3\mathrm{He}, p)\alpha$ nuclear reaction with a 700 keV 3He analysis beam[114].

DiMES had been used to measure the net erosion rate of carbon, which was used to benchmark a modeling code; show that divertor detachment can significantly reduce net carbon erosion; identify the importance of chamber wall aging in chemical sputtering; and observe the MHD interactions between the scraped-off layer current in a tokamak between liquid lithium and SOL plasma.

DiMES has added the capability of temperature control by heating the sample, which has been shown to affect deposition. DiMES been used to study carbon deposition in gaps[117]. DiMES has been used in studying the artificial introduction of characterized carbon dust, migration of dust from the divertor and its transport to the plasma core at 1-2% efficiency[118]. A specially designed porous plug experiment to study the injection of methane at the divertor is being used to benchmark chemical sputtering diagnostics[119],

A midplane material evaluation sample exposure capability (MiMES) is being added by affixing samples to the barrel of a midplane plunging Langmuir probe, with an airlock for changing samples.

B. Quartz microbalances

Quartz microbalances (qmbs) are used to measure fundamental processes of plasma surface interactions – deposition and erosion. They generate valuable data on material gained and lost from discharge to discharge at well defined locations in low heat flux

areas. These measurements can be used to challenge models of dynamic retention and erosion/deposition and advance a predictive understanding of processes occurring at the vessel wall.

The data supplements that measured by witness coupons or tiles that are analyzed after retrieval from a tokamak following an experimental campaign. The coupon data provide well defined spatial information, but the data is integrated over the many different plasma conditions of the campaign so its interpretation is difficult. Alternatively the uptake and degassing of deuterium by the vessel walls can be quantified by measuring the amount of deuterium fuel and the plasma exhaust. This data has time resolution, but no spatial information. Both these techniques have been applied to critical measurements of tritium retention and in one case good agreement was found[120]. More often, limitations to these techniques produce disagreements in retention estimates from these independent techniques. In contrast to these two techniques, qmbs have the advantage of both a well defined spatial location and time resolution. However their spatial coverage is limited as they cannot be used in high heat flux areas, also they cannot resolve changes during a discharge.

Quartz crystal microbalances have been widely used for over 30 years in industry to monitor the growth of thin films in real time during vacuum deposition[121,122,123]. A voltage applied across the faces of a piezoelectric crystal distorts the crystal in proportion to the applied voltage. At certain discrete frequencies a condition of very sharp electro-mechanical resonance is encountered. The lowest frequency response is primarily a 'thickness shear' mode that is called the fundamental. When mass is added to the face of a resonating quartz crystal the frequency of the resonance is reduced. For example, when a 1 Å layer of aluminum is added to a crystal with starting frequency of 6.0 MHz, it will display a reduction of its frequency of 2.27 Hz. The frequency can be measured to an accuracy of 0.1 Hz at a rate 4 times per second, thus the instrument is exquisitely

sensitive to coatings of less than one monolayer. For coatings up to about 10,000 angstroms the thickness is linearly related to the frequency change. Above 10,000 angstroms one needs to take into account the acoustic properties of both the resonating quartz and the thick deposited layer by the so-called Z-match technique[121].

One complication is that the crystal resonant frequency also changes with temperature. The change is non linear and at room temperature the frequency change due to a 1 degree temperature change is equivalent to that due to a few angstrom increase in layer thickness. This effect may be measured separately by a second crystal that is shielded from deposition but exposed to the same temperature changes as the active crystal. The difference in frequencies then represents the change due to deposition. Alternatively a thermocouple can be used to track the temperature and the temperature induced frequency change subtracted.

To date, the electrical and thermal stresses during a plasma discharge have prevented a real time measurement of deposition during a discharge, but the absolute crystal frequency is recovered after a discharge and the change in layer thickness obtained on a discharge-by-discharge basis. The qmb's are not sensitive to dust[124]. Acoustic coupling between the layer and crystal is necessary for a frequency change, simply adding particles to the crystal surface does not change the frequency.

Qmbs were first applied to diagnose plasma-wall interactions in the TdeV tokamak and measured the dependence of deposition on plasma current and plasma detachment[125]. Two qmb's were installed in ASDEX Upgrade[126,127] and showed a significant correlation of deposition with heating power and carbon content of the scrape-off layer. TEXTOR measured a deposition rate of ≈ 30 nm/h at the bottom of the pump duct using a qmb[128]. A commercially available qmb was adapted to the harsh constraints and requirements of JET to investigate the strong tritium retention that had been observed during the DTE1

campaign[129,130]. A strong increase of deposition with decreasing distance of the strike point position to the louver entrance was found and it was shown that ELMy H-mode discharges with the strike point on the horizontal target dominated the carbon layer formation. Two qmbs were installed on NSTX to investigate deposition in a location remote from the plasma that mimicked a typical diagnostic window or mirror. A rear facing quartz crystal recorded deposition of lower sticking probability molecules at 10% of the rate of the front facing one. Time resolved measurements over a 4-week period with 497 discharges, recorded 29.2 $\mu g/cm^2$ of deposition, however surprisingly, 15.9 $\mu g/cm^2$ of material loss occurred at 7 discharges. The net deposited mass of 13.3 $\mu g/cm^2$ matched the mass of 13.5 $\mu g/cm^2$ measured independently by ion beam analysis[131]. Interestingly, a slow rise in deposition in the inter-pulse period was observed and it was suggested that this may be related to the condensation of polymer-like films

after each discharge. More recently the NSTX qmbs have been moved closer to the plasma and have measured mass gain and loss due to dynamic retention of deuterium[132].

VII. DUST MEASUREMENTS

A. Importance of dust; electrostatic dust detectors

Diagnosis and management of dust particles in tokamaks is a 'housekeeping' area that falls in-between traditional plasma diagnostics and plasma technology fields, however it is critical to the safe operation of next step devices. Dust has not been a noticeable problem so far in current fusion devices, however, in next step devices such as ITER, the increase in duty cycle and erosion levels will cause a large scale-up in the amount of particles produced and this has important safety consequences[133]. Tokamak dust may be radioactive from tritium or activated metals, toxic and /or chemically reactive with steam or air. The large surface area associated with dust can greatly amplify its chemical reactivity. Tritiated dust becomes statically charged through the emission of beta electrons and this enhances its mobility[134]. The in-vessel particle inventory must be regulated so it cannot create a safety hazard. A guideline to limit the mobilisable tungsten dust to 100 kg inside the ITER vacuum vessel has been established due to its radiological hazard. To limit the hydrogen potentially generated by chemical reactions following in-vessel coolant spills or air ingress a limit of 6 kg each of beryllium, carbon and tungsten dust on hot plasma facing components of the divertor was proposed[135] however it is not clear that a corresponding measurement is practical. Recent calculations have highlighted the mobility of dust particles in the electric and magnetic fields of a tokamak and the possibility of plasma contamination from mobile dust[136]. Measuring the dust particle inventory is a challenge in existing tokamaks (sect. VIIf) let alone one with the radiological environment and scale of ITER[137-139]. A separate challenge is demonstrating techniques that could remove dust from the tokamak, once the limits are approached.

An ideal diagnostic would produce a complete spatial map of the areal density of dust and its particle size distribution throughout the tokamak and demonstrate continuous compliance with the dust inventory limits during plasma operations. However, such a diagnostic does not exist. Quartz microbalances have recently been applied to measuring deposition in tokamaks, but a simple test depositing 17 mg of carbon particles on the quartz crystal showed a complete lack of response (less than 0.01 μg) presumably due to the lack of mechanical coupling between the particles and quartz crystal.

A novel device to detect dust particles that shows promise for the detection of conductive dust settling in remote inaccessible areas in fusion devices has recently been developed in the laboratory[140,141]. Two closely interlocking grids of conductive traces on a circuit board were biased to 30 – 50 V. Test particles, scraped from a carbon fiber composite tile, were delivered to the grid by a stream of nitrogen. Miniature sparks appeared when the particles landed on the energised grid and created a transient short circuit. Typically the particles vaporized in a few seconds restoring the previous voltage standoff. The transient current flowing through the short circuit created a voltage pulse that was recorded by standard nuclear counting electronics. The device worked well in both at atmosphere and in vacuum environments and showed a clear correlation between the recorded counts and particle concentration. The sensitivity was enhanced by more than an order of magnitude by the use of ultrafine grids (25 μm spacing)[142]. The response to particles of different size categories was compared and the sensitivity, expressed in counts / areal density (mg/cm^2) of particles, was maximal for the finest particles. This is a favorable property for tokamak dust which is predominantly of micron scale. Qualitative information on the size of the particles is apparent in the current pulse created by the short circuit.

Impinging dust particles are detected when they create a short circuit between the traces, however this short circuit is temporary suggesting the device may be useful for the

removal of dust from specific areas. The fate of the dust particles has been tracked by measurements of mass gain / loss. Heating by the current pulse caused up to 90% of the particles to be ejected from the grid or vaporized, the removal efficiency depending on the experimental geometry[143]. One could envisage a large area mosaic of these devices that would ensure that specific areas remained dust free. Nanoengineered traces on a low activation substrate such as SiO_2 could be applied to detect metallic or mixed material dust in an activated environment. Further development is in progress to test these possibilities.

Dust has previously been collected from NSTX during a maintenance period and characterized[144]. Real-time measurements were attempted by installing two grids in NSTX on a vertical port 60 cm below the outer divertor at Bay C together with a glass slide to passively collect dust. It turned out that the flux of dust in NSTX 5.6 ng/cm^2/discharge was below the estimated sensitivity of 36 ng/cm^2/count of the present grid detector. A large area detector is planned to increase the sensitivity and permit measurements on current tokamaks. We note that the ITER dust limit of 100 kg evenly distributed on the lower part of the machine amounts to ~ 60 mg/cm^2 so sensitivity will not be an issue for ITER.

Acknowledgments

This is a report of work supported by the U.S. Department of Energy under Cooperative Agreement DE-FC02-04ER54698, W-7405-ENG-48, DE-FG02-04ER54762, DE-FG02-04ER54758, DE-AC04-94AL85000, DE-FG02-04ER54758, and performed in the framework of bilateral US-EURATOM Exchange program.

References

SECTION 1

[1] C.J. Lasnier, D.N. Hill, T.W. Petrie, A.W. Leonard, T.E. Evans, R. Maingi, Nucl. Fusion **8**, 1225 (1998).

[2] S. Clement, A. Chankin, D. Ciric, J.P. Coad, J. Falter, E, Gauthier, J. Lingertat, S. Puppin, J. Nucl. Mater **266-269**, 285 (1999).

[3] T.W. Petrie et al., Proc. 18th Euro Conf. on Controlled Fusion and Plasma Physics, Berlin, Vol. **3**, 237 (1991).

[4] T.W. Petrie, D. Buchenauer, D.N. Hill, *et al.*, J. Nucl Mater **196-198**, 848 (1992).

[5] S.L. Allen, N.H. Brooks, R.B. Campbell, *et al.*, J. Nucl. Mater. **220–222**, 336 (1995).

[6] C.J. Lasnier, K.H. Burrell, J.S. deGrassie, A.W. Leonard, R.A. Moyer, G.D. Porter, J.G. Watkins, DIII-D team, J. Nucl. Mater. **313-316**, 904-908 (2003).

[7] M.E. Fenstermacher, *et al.*, "A tangentially viewing visible TV system for the DIII-D divertor," Rev. Sci. Instrum. **68**, 348 (1997).

[8] A. Maas, *et al.*, "Diagnostic experience during the deuterium-tritium experiments in JET, techniques and measurements," JET pre-print JET-P, 80 (98).

[9] K. Itami, *et al.*, "Observation of detachment in the JET MkIIGB divertor using CCD camera tomography," J. Nucl. Mat. **290-293**, 633 (2001).

[10] J. Gafert, *et al.*, "Determination of 2D-Emissivity-Distributions from a digital 12-bit CCD system viewing the divertor of ASDEX Upgrade tangentially and poloidally," Proc. 29th EPS conference on Contr. Fusion and Plasma Physics, Montreux, Switzerland, 17-21 June, 2002, ECA Vol. **26B** P1, 123 (2002).

[11] J. Gafert, *et al.*, "Reconstruction of the two-dimensional emissivity distributions in the ASDEX Upgrade LYRA-Divertor from TV-CCD-Data," Proc. 26th EPS

conference on Contr. Fusion and Plasma Physics, Maastricht, The Netherlands, 14-18 June, 1999, ECA Vol. **23J**, 1577 (1999).

[12] M.E. Fenstermacher, *et al.*, "The two-dimensional structure of radiative divertor plasmas in the DIII-D tokamak," Phys. Plasmas **4**, 1761 (1997) [also "Comprehensive 2D measurements of the radiative divertor plasma in DIII-D," J. Nucl. Mat. **241-243**, 666 (1997)].

[13] M.E. Fenstermacher, *et a*l., "Evolution of 2D deuterium and impurity radiation profiles during transitions from attached to detached divertor operation in DIII-D," J. Nucl. Mat. **266-269**, 348 (1999).

[14] A. Huber, *et al.*, "Tomographic reconstruction of 2D line radiation distribution in the JET MkIIGB divertor," J. Nucl. Mat. **313-316**, 925 (2003).

[15] C.J. Boswell, *et al.*, "Applications of visible CCD cameras on the Alcator C-mode tokamak," Rev. Sci. Instrum. **72**, 935 (2001).

[16] R.A. Pitts, *et al.* "Divertor geometry effect on detachment in TCV," J. Nucl. Mat. **290-293**, 940 (2001) (also R.A. Pitts, *et al.*, "Detachment in variable divertor geometry on TCV," 18th IAEA Fusion Energy Conference, Sorrento, Italy, 4-10 October, 2000, IAEA-CN-77/EXP4/23).

[17] M. Groth, *et al.*, "Assessment of the poloidal distribution of core plasma fueling and impurity sources in DIII-D," J. Nucl. Mat. **337-339**, 425 (2005).

[18] S.L. Allen, *et al.*, "13C transport studies in L-mode divertor plasmas on DIII-D," J. Nucl. Mat. **337-339**, 337 (2005).

[19] M. Groth, *et al.*, "Diagnosis of edge localized mode evolution in DIII-D using fast-gated CID and infrared cameras," Rev. Sci. Instrum. **74**, 2064 (2003).

[20] A. Sykes, *et al.*, "First results from MAST," Nucl. Fusion **41**, 1423 (2001).

[21] S.J. Zweben, *et al.*, "Edge turbulence imaging in the Alcator C-mod tokamak," Phys. Plasmas **9**, 1981 (2002).

[22] A.L. Roquemore, *et al.*, "NSTX tangential divertor camera," Rev. Sci. Instrum. **75**, 4190 (2004).

[23] S.J. Zweben, *et al.*, "Edge turbulence imaging in the Alcator C-mod tokamak," Phys. Plasmas **9**, 1981 (2002).

[24] R.J. Maqueda, *et al.*, "Gas puff imaging of edge turbulence," Rev. Sci. Instrum. **74**, 2020 (2003).

[25] S.J. Zweben, *et al.*, "High-speed imaging of the edge turbulence in NSTX," Nucl. Fusion **44**, 134 (2004).

[26] M. Groth, *et al.*, "High time-resolved, 2D imaging of type-I ELMs in DIII-D using an image-intensified CID camera," J. Nucl. Mat. **313-316**, 1071 (2003).

[27] M.E. Fenstermacher, *et al.*, "Structure, stability, and ELM dynamics of the H-mode pedestal in DIII-D," 20th IAEA Fusion Energy Conference, Vilamoura, Portugal, 1-6 November, 2004, IAEA-CN-116/EX/2-5Rb.

[28] E.M. Hollmann, *et al.*, "Measurement of impurity and heat dynamics during noble gas jet-initiated fast plasma shutdown for disruption mitigation in DIII-D," 20th IAEA Fusion Energy Conference, Vilamoura, Portugal, 1-6 November, 2004, IAEA-CN-116/EX/10-6Ra.

[29] D.G. Nilson, *et al.*, "A tangentially viewing vacuum ultraviolet TV system for the DIII-D divertor," Rev. Sci. Instrum., **70**, 738 (1999).

[30] M.E. Fenstermacher, *et al.*, "Evolution of 2D Visible and VUV Divertor Emission Profiles During DIII-D H-mode Detachment Transitions," Proc. 26th European Physical Society Conference on Controlled Fusion and Plasma Physics, Maastricht, The Netherlands, 14-18 June 1999.

[31] N.W. Jalufka, *et al.*, "Profiles of 155 nm CIV Radiation in a Radiative Divertor Plasma in DIII-D," Bull. Am. Phys. Soc., **43**, 1889 (1998).

[32] N.W. Jalufka, *et al.*, "Poloidal Profile of CIV Emission in the DIII-D Divertor During PDD Operation," Bull. Am. Phys. Soc., **44**, 170 (2000).

[33] R.D. Wood, *et al.*, "Measurements of Divertor Impurity Concentrations on DIII-D," Proc. of the 23rd European Physical Society Conference on Contr. Fusion and Plasma Phys., Kiev, Ukraine (1996).

[34] R.D. Wood, *et al.*, "Measurement of Divertor Radiated Power Losses in the 17-170 nm Spectral Region on DIII-D," Bull. Am. Phys Soc., **42**, 1844 (1997).

[35] D.G. Whyte, B.L. Lipschultz, P.C. Stangeby, J. Boedo, D.L. Rudakov, J.G. Watkins, W.P. West, "The magnitude of plasma flux to the main wall in the DIII-D tokamak," Plasma Phys. Contr. Fusion (in press).

[36] Haas G, Gernhardt J, Keilhacker M, Meservey E B and the ASDEX Team, J. Nucl. Mater. **121,** 151 (1984).

[37] J.F. O'Hanlon, A User's Guide to Vacuum Technology (J. Wiley & Sons, New York, 1980), Section 3.2, Vacuum Physics and Technology, Vol. **14** of Methods of Experimental Physics series, (Academic Press, Orlando, 1979), Section 2.4.

[38] IPT-Albrecht GmbH, www.ipt-albrecht.de.

[39] MKS Instruments Inc., www.mksinst.com/PMC1.html.

[40] K.H. Finken, K.H. Dippel, W.Y. Baek and A. Hardtke, "Measurement of Helium Gas in a Deuterium Environment," Rev. Sci Instrum. **63**, 1-7 (1992).

[41] D.L Hillis, P.D. Morgan, J.K. Ehrenberg, M.F. Stamp, M. von Hellerman and V. Kumar, "Tritium Concentration Measurements in the Joint European Torus by Optical Spectroscopy of a Penning Gauge," Rev. Sci. Instrum. **70**, 359-362 (1999).

[42] D. Lichtman, "Perspectives on residual gas analysis," J. Vac. Sci. Technol. **A 2,** 200-205 (1984).

[43] C. Tilford, "Process monitoring with residual gas analyzers (RGAs): limiting factors," Surf. Coat. Technol. **68/69,** 708 (1994).

[44] W. Paul and M. Raether, Z. Physik **140,** 262 (1955).

[45] J.A. Basford, M.D. Boeckmann, R.E. Ellefson, A.R. Filippelli, D.H. Holkeboer, L. Lieszkovszky, C.M. Stupak, "Recommended practice for the calibration of mass

spectrometers for partial pressure analysis," J. Vac. Sci. Technol. **A 11,** 22-40 (1993).

[46] G.L. Jackson, "The leak testing program of the doublet III project," J. Vac. Sci. Technol., **20**, 1182-1187 (1982).

[47] K.L. Holtrop, "Outgassing tests on materials used in the DIII-D magnetic fusion tokamak," J. Vac. Sci. Technol. **A 17,** 2064-2068 (1999).

[48] A. McLean, "13CH4 injection studies in DIII-D: the tritium retention issue," presentation E03.008 to APS 2004.

[49] J.A. Goetz, *et al.*, "Impurity compression and enrichment studies on Alcator C-MOD," J. Nucl. Mater. **266-269,** 354-359 (1999).

[50] Y. Yang, *et al.*, "Hydrogen retention during long discharges in HT-7 superconducting tokamak," invited presentation I-12 to PSI 16, 2004 (to be published).

[51] S. Hiroki, *et al.*, "Leak detection system in ITER," Fusion Eng. And Design **46,** 11-26 (1999).

[52] R. Pearce, et al., "Operational experience with a remote radiation hard quadrupole residual gas analyzer," Vacuum **44,** 643-645 (1993).

[53] K. Itoh, S.I. Itoh, M. Yagi and A. Fukuyama, Plasma Phys. and Control. Fusion **1**, (1996).

[54] Ch. Ritz, H. Lin, T.L. Rhodes, and A.J. Wooton, Phys. Rev. Lett. **65**, 2543 (1990).

[55] T.L. Rhodes, C.P. Ritz, R.D. Bengtson and K. Carter, Rev. Sci. Instrum. **61**, 3001 (1990).

[56] R. Moyer, et al, Phys. Plasmas **2**, 2397 (1995).

[57] W. Rowan, et al., Nucl. Fusion **2**, 1105 (1987).

[58] G.R. Tynan, et al, Phys. Plasmas **1** 3301 (1994).

[59] T.L. Rhodes, C.P. Ritz and R.D. Bengtson, Nucl. Fusion **33**, 1147 (1993).

[60] P.C. Stangeby and G.M. McCracken, Nucl. Fusion **30**, 1225 (1990).

[61] P.C. Stangeby, J.D. Elder, J.A. Boedo, B. Bray, N.H. Brooks, M.E. Fenstermacher, et al. Journal of Nuclear Materials **313-316**, 883-7 (2003).

[62] X.Q. Xu, R.H. Cohen, W.M. Nevins, G.D. Porter, M.E. Rensink, T.D. Rognlien, et al. Nucl. Fusion **42** (1), 21-7 (2002).

[63] G.D. Porter, R. Isler, J. Boedo, T.D. Rognlien, Phys. Plasmas **7** (9), 3663-80 (2000).

[64] A.S. Kukushkin, H.D. Pacher, G.W. Pacher, G. Janeschitz, D. Coster, A. Loarte, D, Reiter, Nucl. Fusion **43** (8), 716-23 (2003).

[65] D. Reiter, S. Wiesen, M. Born, J. Nucl. Mater. **313-316**, 845-51 (2003).

[66] S.S. Zweben, P.C. Liewer, Gould J. Nucl. Mater. **111-112**, 39 (1982).

[67] B. La Bombard, B. Lipshultz, Nucl. Fusion **27**, 81 (1987).

[68] R.A. Moyer, J. Watkins, et al. Rev. Sci. Instruments, (1995).

[69] J. Watkins, et al. Rev. Sci. Instrum. **3**, 4728 (1992).

[70] J.A. Boedo, D.S. Gray, et al., Rev. Sci. Instrum. **69** (7) 2663 (1998).

[71] J.A. Boedo, D.S. Gray, R. Ivanov, A.V. Chernilevsky, J. Schwelberger, K.H. Finken, G. Mank, G. Van Oost and the TEXTOR Team, Proceedings EPS Bournemouth, Vol. **1** I-293 (1995).

[72] J.A. Boedo, D.S. Gray, et al, Submitted to Nucl. Fusion. (1998).

[73] S. Erents, S.A. Tagle, G.M. Mc Cracken, Nucl. Fusion **26** (12) 1591 (1986).

[74] R. Conn , et al., Proc. Am. Phys. Soc. **34**, 1986 (1989).

[75] A.S. Wooton, M.E. Austin, R.D. Bengtson, et al., Plasma Phys. and Control. Fusion **30** (11), 1479 (1988).

[76] D. Bora, R. Ivanov, G. Van Oost, U. Samm, Nucl. Fusion **31** 2383 (1991).

[77] H. Lin, R.D. Bengston, C.P. Ritz, Phys. Fluids **1** (10) 2027 (1989).

[78] V.P. Budaev and R.S. Ivanov, J. Nucl. Mater. **162-1614** 322 (1989).

[79] C. Hidalgo, C. Pardo, B. Zurro, et al., Preprint IAEA-CN-56/a-4-31(c) (1992).

[80] C. Hidalgo, R. Balbin, M.A. Pedrosa, I. Garcia-Cortes and M.A. Ochando, Phys.

Rev. Lett. **69** (8) 1205 (1992).

[81] H. Lin, G.X. Li, R.D. Bengtson, Ch.P. Ritz and H.Y.W. Tsui, Rev. Sci. Instrum. **63** (10), 4611 (1992).

[82] Liewer, McChesney, Zweben and Gould, Phys. Fluids **29** 309 (1986).

[83] Sin-Li Chen and T. Sekiguchi, J. Appl. Phys. **36** (8), 2363 (1965).

[84] G.F. Matthews, et al., J. Nucl. Mater. **145-147** 225 (1987).

[85] G. Proudfoot and P.J. Harbour, J. Nucl. Mater. **93-94** (1980).

[86] T.N. Todd, Journal de Physique (suppl. to No. 7) **40,** C7-84 (1979).

[87] R. Van Nieuwehove, G. Van Oost, Rev. Sci. Instrum. **59** (7) 1053 (1988).

[88] L. Bogomolov, R. Ivanov, A. Chernilevsky, et al., Sov. J. Plasma Phys. **18** (6), 679 (1992).

[89] R.S. Ivanov, A.N. Chernilevsky, U. Samm, R. van Nieuwenhove and G. van Oost, Phys. Lett. A **173** 288-292 (1993).

[90] Handbook of Mathematical Functions, M. Abramowitz, Page 376, Eq. 9.6.34, Dover (1972).

[91] R.A. Pitts and P.C. Stangeby, PPCF **32** 1237 (1990).

[92] J G. Watkins, et al., Rev. Sci. Instrum **3**, 4728 (1992).

[93] J.G. Watkins, et al., Rev. Sci. Instrum **68**, 373 (1997).

[94] J.A. Boedo, D. Gray, L. Chousal, et al, Rev. Sci. Instrum. **69** (7) 2663 (1997).

[95] C. Neumeyer, P. Heitzenroeder, J. Spitzer, J. Chrzanowski, A. Brooks, J. Bialek, et al., *Fusion Engineering & Design* **54 (**2), 275-319 (2001).

[96] J. Boedo, L. Chousal, et al., Submitted to Rev Sci. Inst. (2006).

[97] P.W. Hait, et al., 13th Vacuum Symposium of the American Vacuum Society, **1**, 678 (1996).

[98] R. Pitts, et al., Nucl. Fusion **30**, 789 (1990).

[99] D.S. Gray, J. Boedo, R. Conn, et al., Phys. Plasmas, (1998).

[100] A.H. Nielsen, H.L. Pecsell, and J. Juul Rasmussen, Phys. Plasmas **3**, 1530 (1996).

[101] R.A. Moyer, R.D. Lehmer, T.E. Evans, *et al*., Plasma Phys. Control. Fusion **38**, 1273 (1996).

[102] J.A. Boedo, D.L. Rudakov, R.A. Moyer, S. Krashenninikov, *et al*., Phys. Plasmas **8**, 4826 (2002).

[103] S.J. Zweben, R.J. Maqueda, D.P. Stotler, A. Keesee, J. Boedo, C.E. Bush, Nucl. Fusion **43** 1–20 (2003).

[104] M. Baelmans, D. Reiter, R.R. Weynants, et al., J. Nucl. Mater. **1** 446 (1992).

[105] P.C. Liewer, J.M. McChesney, S.J. Zweben and R.W. Gould, Phys. Fluids 2, 309 (1986) 309.

[106] E.J. Powers, Nucl. Fusion **1** 749 (1974).

[107] V. Riccardo, W. Fundamenski, and G.F. Matthews, Plasma Phys. Control. Fusion **43**, 881 (2001).

[108] J.G Watkins, C.J. Lasnier, *et al*, Rev. Sci. Instrum. **74**, 1574 (2003).

[109] S. Gangadhara, B. LaBombard, B. Lipschultz, and N. Pierce, Bull. Am. Phys. Soc. **41**, 1550 (1996).

[110] The Self-Renewing Thermocouple, (Nanmac Corp., Framingham, MA).

[111] C.P.C. Wong, R. Junge, R.D. Phelps et al., "Divertor materials evaluation system at DIII-D," J. Nucl. Mater. **196-198,** 871-875 (1992).

[112] D.G. Whyte, M.R. Wade, D.F. Finkenthal, et al., "Measurement and verification of Z_{eff} radial profiles using charge exchange recombination spectroscopy on DIII-D," Nuclear Fusion **38** (3), (1997).

[113] D.R. Whyte, J.N. Brooks, C.P.C. Wong, et al., "DiMES divertor erosion experiments on DIII-D," J. Nucl. Mater. **241-243,** 660-665 (1997).

[114] W.R. Wampler, R. Bastasz, D. Buchenauer, "Erosion and deposition of metals and carbon in the DIII-D divertor," J. Nucl. Mater. 2**33-237,** 791-797 (1996).

[115] R. Bastasz, W.R. Wampler and J.W. Cuthbertson, et al., "Measurements of carbon and tungsten erosion/deposition in the DIII-D divertor, J. Nucl. Mater., **220-222**, 310-314 (1995).

[116] D.G. Whyte, R. Bastasz, J. N. Brooks, et al., "Divertor erosion in DIII-D", J. Nucl. Mater. **266-269**, 67-74 (1999).

[117] Krieger, 17th PSI.

[118] D.L. Rudakov-dust Rudakov, J.A. Boedo, R.A. Moyer, et al., 16th HTPD conference, Williamsburg, Virgina May 7-11, 2006 to be published.

[119] A.G. McLean, J.W. Davis, P.C. Stangeby, et al., PSI-17.

[120] C. H. Skinner, et al., J. Nucl. Mater. **290 -293**, 486 (2001).

[121] C.S. Lu and O. Lewis, J. Appl. Phys. **43**, 4385 (1972).

[122] J. Janata, Principles of Chemical Sensors (Plenum Press, New York, 1990) p.55.

[123] Inficon Technical Note "The technology of the intelligent oscillator for quartz crystal measurement" Inficon, Two Technology Place, East Syracuse, NY 13057.

[124] A. Bader, C.H. Skinner, A.L. Roquemore, and S. Langish, Rev. Sci. Instrum. **75**, 370 (2004).

[125] D. Bourgoin, G.G. Ross. S. Savoie, Y. Drolet, E. Haddad., J. Nucl. Mater. **241-243** 765 (1997).

[126] V. Rhode, H. Maier, K. Krieger, R. Neu, J. Perchermaier, J. Nucl. Mater. **290-293** 317 (2001).

[127] V. Rohde, et al., Phys. Scr., T **102**, 25 (2003).

[128] J. von Seggern, et al., J. Nucl. Mater. **313-316,** 439-443 (2003).

[129] H.G. Esser, et al., Fusion Eng. Des. **66-68,** 855 (2003).

[130] H.G. Esser, V. Philipps, M. Freisinger, P Coad, G.F. Matthews, G. Neil, Phys. Scr., T **111**, 129 (2004).

[131] C.H. Skinner, H. Kugel, A.L. Roquemore, J. Hogan W. Wampler and the NSTX team. J. Nucl. Mater. **337-339**, 129-133 (2005).

[132] C.H. Skinner, H.W. Kugel, A.L. Roquemore, R. Maingi, W.R. Wampler, "Pulse-by-pulse measurements of dynamic retention and deposition in NSTX," 17th International Conference on Plasma Surface Interactions, Hefei, China, May 22-26, 2006, submitted to J. Nucl. Mater.

[133] G. Federici, C.H. Skinner, J.N. Brooks, J.P. Coad, C. Grisolia, A.A. Haasz, A. Hassanein, V. Philipps, C.S. Pitcher, J. Roth, W.R. Wampler, D.G. Whyte, Nucl. Fus. **41,** 1967 (2001).

[134] C.H. Skinner, C.A. Gentile, L. Ciebiera, S. Langish, Fus. Sci. & Technol. in press (2003).

[135] '*Radiological source terms'*, Chapt. 5.3, p. 13, in ITER Technical Basis, ITER EDA Documentation Series No. 24, IAEA, Vienna (2002).

[136] S.I. Krasheninnikov, Y. Tomita, R.D. Smirnov, R.K. Janev, Phys. Plasmas, **11,** 3141, (2004).

[137] G.F. Counsell and C.H. Wu, Phys. Scripta. **TIC116**, 1 (2001).

[138] R. Reichle, et al., J. Nucl. Mater. **290-293**, 701 (2001).

[139] G.T. Razdobarin, G. Federici, V.M. Kozhevin, E.E. Mukhin, V.V. Semenov, S.Y. Tolstyakov, Fusion Sci. & Technol. **41**, 32-43 (2002).

[140] A. Bader, C.H. Skinner, A.L. Roquemore, and S. Langish, Rev. Sci. Instrum. **75**, 370 (2004).

[141] C.H. Skinner, A.L. Roquemore, A. Bader and W.R. Wampler, Rev. Sci. Instrum. **75** 4213 (2004).

[142] C. Vonier, C.H. Skinner, A.L. Roquemore, J. Nucl. Mater. **345** 266 (2005).

[143] C.V. Parker, C.H. Skinner and A.L. Roquemore, 17th International Conference on Plasma Surface Interactions, Hefei, China, May 22-26,2006, submitted to J. Nucl. Mater. (2006).

[144] J.P. Sharpe, et al., J. Nucl. Mater. **337-339** 1000 (2005).

TABLE I. Plasma species and their transition wavelengths typically measured with visible cameras in present fusion experiment.

Plasma species	Transition wavelength
Deuterium	Atomic: D_α (656 nm), D_γ (434 nm), molecular: 602 nm
Carbon	Neutral: CI (834 nm, 910 nm), singly ionized: CII (514 nm), doubly ionized: CIII (465nm), radical: CH/CD (431 nm)
Helium	Neutral: He I (706 nm), singly ionized: He II (468 nm)
Neon	Neutral: Ne I (640 nm)
Argon	Neutral: Ar I (696 nm), singly ionized: Ar II (612 nm)

List of Figure Captions

Fig. 1. Up-down power distribution. (a) Percent difference between peak power to lower and upper divertor, versus the distance at the midplane between the flux surfaces on which the lower and upper X–points lay.

Fig. 2. Wide-angle view of NSTX during a kink mode (courtesy C.E. Bush and R.J. Maqueda).

Fig. 3. A single probe I-V characteristic. Applied voltage is normalized to kTe.

Fig. 4. Schematic of a single probe circuit. The sweeping power supply and voltage and current measurements are referred to ground. The current measurement can be a shunt resistor or an inductive sensor (shown) for isolation.

Fig. 5. Single probe current and voltage. Strong fluctuations in the current can be seen due to strong intermittency in the plasma boundary.

Fig. 6. Schematic of a double probe circuit. Notice that the sweeping power supply and the current and voltage measurements float.

Fig. 7. Double probe current and voltage. The current is symmetric about zero and saturates at the ion saturation current which shows strong intermittency.

Fig. 8. Poloidal cross section of the NSTX device (dashed lines), where a line indicates the vertical location of the probe, slightly below the midplane. A superimposed plasma simulation grid illustrates where the plasma boundaries would be in a double null

configuration. The directions of the current and toroidal field are indicated, as well as the B-drift direction.

Fig. 9. Probe tip and head geometry showing the cut that follows the flux surface geometry. a) side view; b) front view. The tips are labeled according to their function. Tips Vf1 to Vf5 are at floating potential, two tips Double1-2 (bold Te indicates that they will later be implemented as a fast te measurement) are in a double probe configuration, two more tips measure the Mach number of the plasma flow (bold indicates not yet commissioned) and a last tip measures I_{sat}. The toroidal magnetic field B_T is sloping at 35 deg as seen from the inside of the vessel.

Fig. 10. Probe head assembly without the graphite shroud and detail of the BN tip holder, showing the modular construction which allows fast tip replacement. The location of the circuit board is also shown.

Fig. 11. The probe shaft assembly indicating the main components.

Fig. 12. The circuit board geometry, showing schematically the location of sensors resistors and edge connectors.

Fig. 13. Drawing indicating the main probe components. The shaft and propelling piston move on top of a carriage that rides on parallel rails moved by a step motor. The probe system is supported by an aluminum backbone and is electrically insulated in two stages, to prevent possible arcing. A breakout box provides easy access to all the cables and control system interface.

Fig. 14. The probe position (a), velocity (b) and acceleration (c) of the probe vs time are

shown. Time intervals of interest are marked 1 to 5. Interval 1 is when the maximum acceleration occurs, interval 2 is when the maximum velocity is achieved, interval 3 is when the maximum deceleration happens and the beginning of the dwell time and intervals 4 and 5 indicate similar events during the retraction.

Fig. 15. Traces showing double probe current (a) and voltage (b). The sweep frequency is 1 ms and the signals are digitized at 1 MHz. The current signal shows plasma fluctuations and intermittency.

Fig. 16. Power spectrum of the I_{sat} signal showing that most power is in the 0-100 kHz range. The peak power, indicated by an arrow at $\sim 10^{-2}$, resides at very low frequencies.

Fig. 17. The I_{sat} trace (bottom) is shown for a 40 ms interval where the presence of intermittent events is quite clear. A 5 ms interval (top) is magnified so that it can be seen that the intermittent events last ~20-40 ms.

Fig. 18. Traces of electron density vs radial position measured by the double probe for three NSTX discharges. The data is labeled by discharge number, confinement regime (L or H confinement) and heating power in MW. An exponential fit and resulting decay length are also indicated for each trace the longest decay length corresponds to an L-mode discharge. The nominal position of the separatrix is labeled zero. The probe penetrates about 7 mm in the plasma.

Fig. 19. Data traces from divertor heat flux probes (top) and resultant parallel heat flux times in the discharge (bottom). Circled numbers indicate probes' locations on the outer divertor (see Fig. 2).

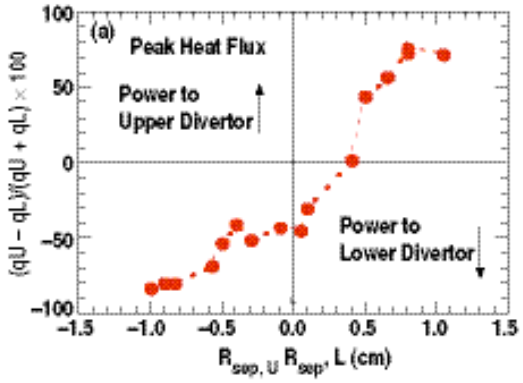

165-06 fig. 1 jy

165-06 lig.1/rs

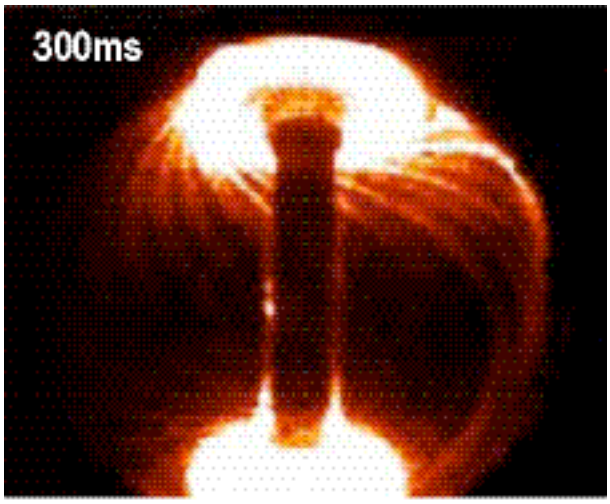

165-06 fig. 2 jy

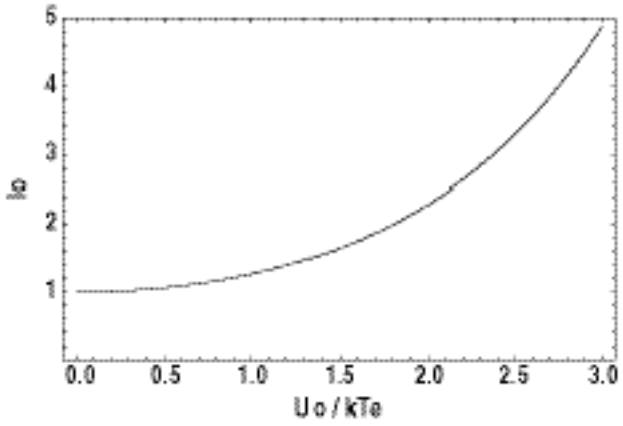

165-06 fig. 3 jy

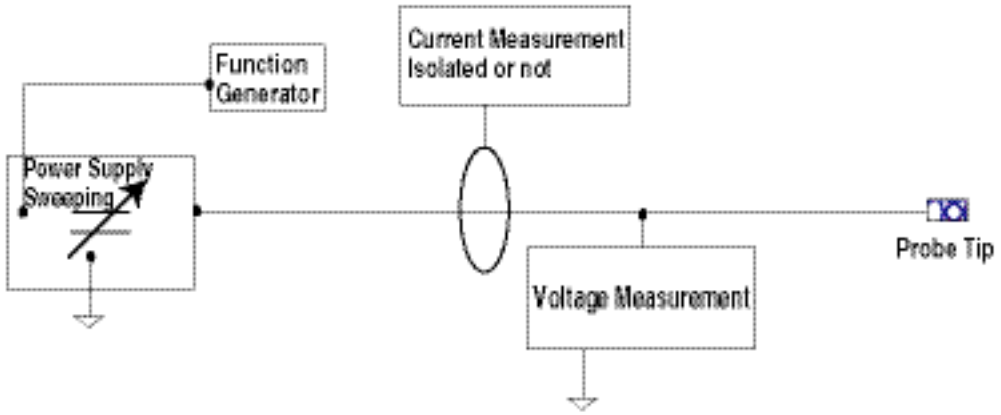

165-06 fig. 4 jy

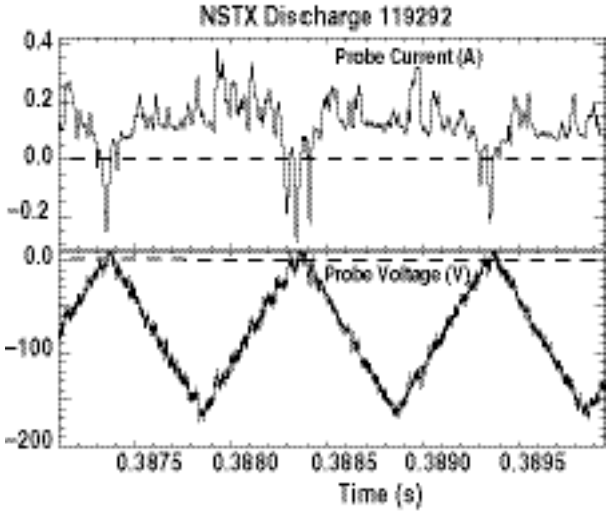

165-06 fig. 5 jy

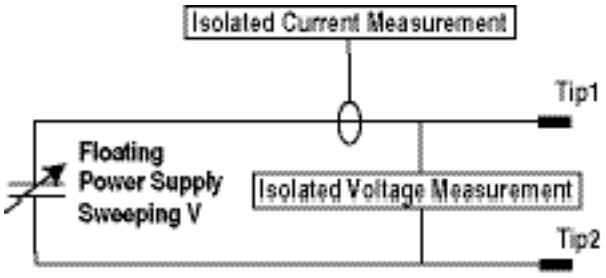

165-06 fig. 6 jy

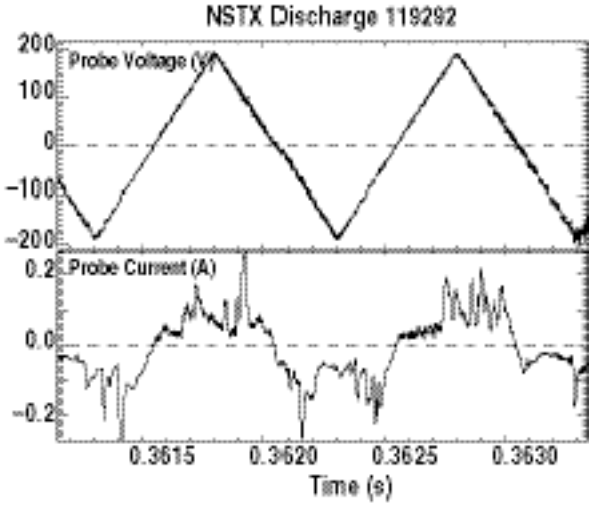

165-06 fig. 7 jy

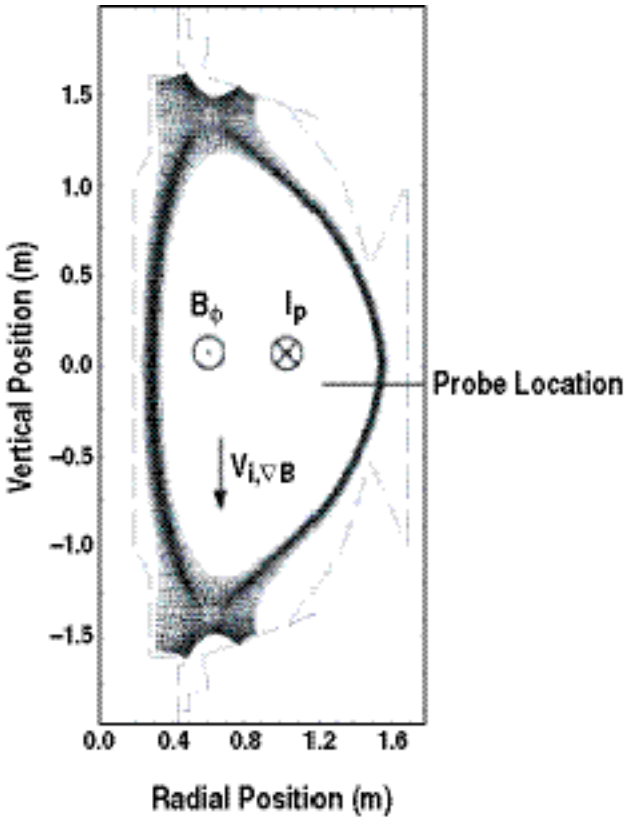

165-06 fig. 8 jy

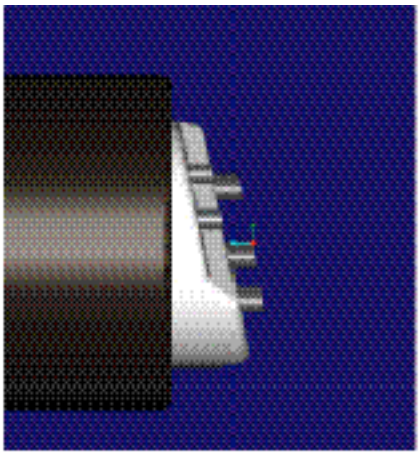

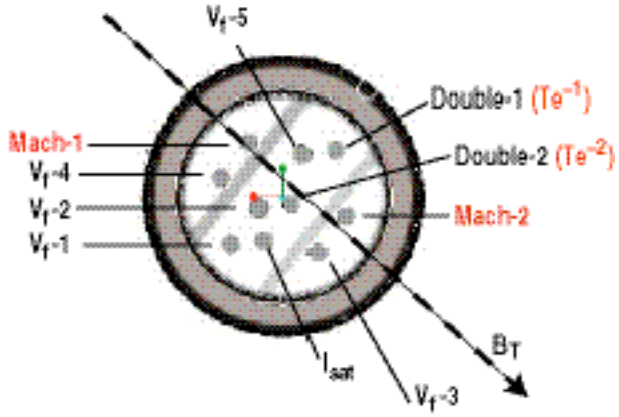

165-06 fig. 9 jy

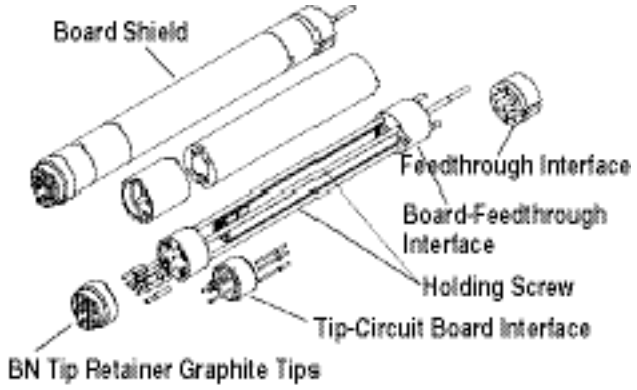

165-06 fig. 10 jy

165-06 fig. 1 jy

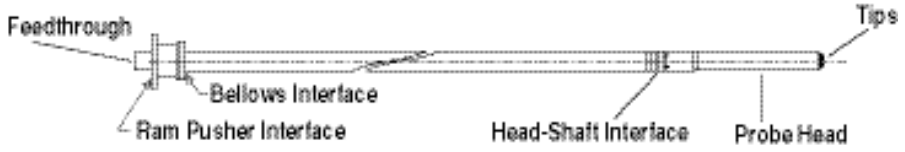

165-06 fig. 11 jy

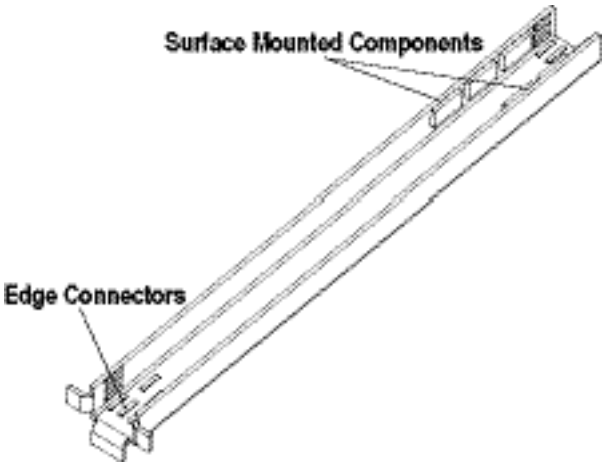
Surface Mounted Components
Edge Connectors

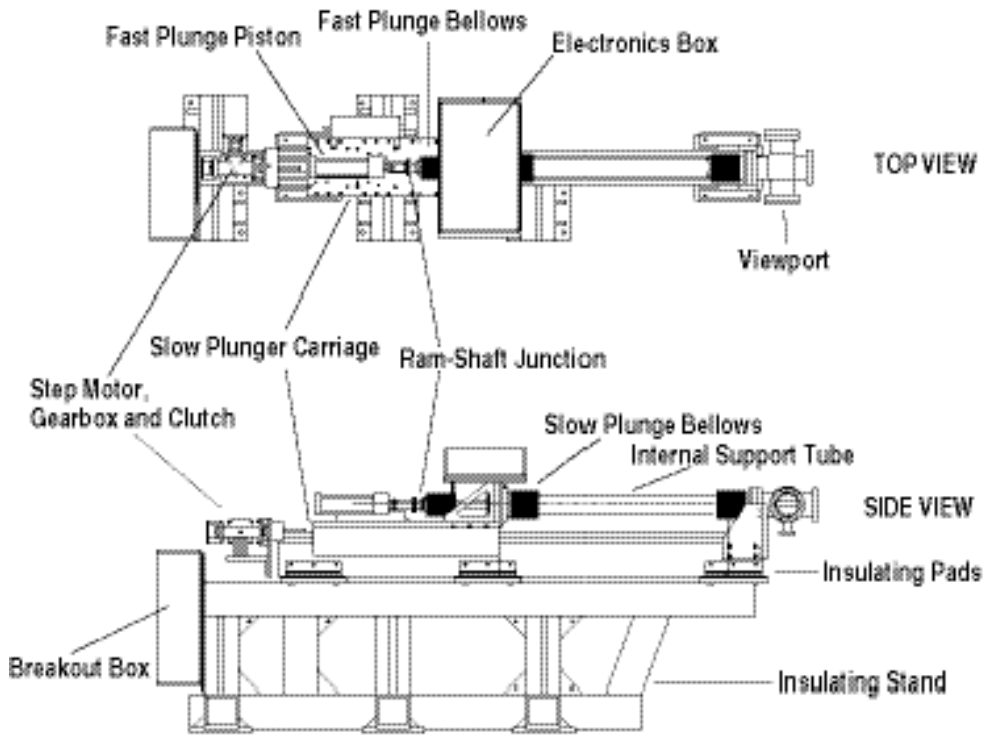

165-06 fig. 13 jy

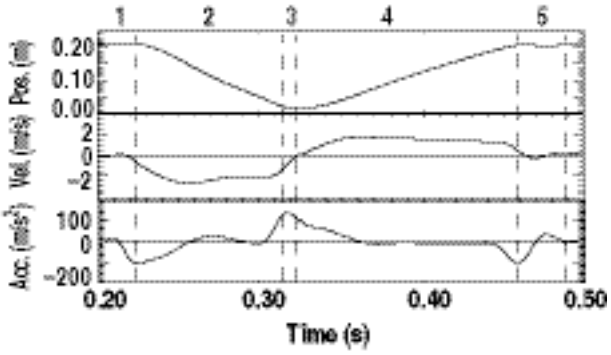

165-D6 fig. 14 jy

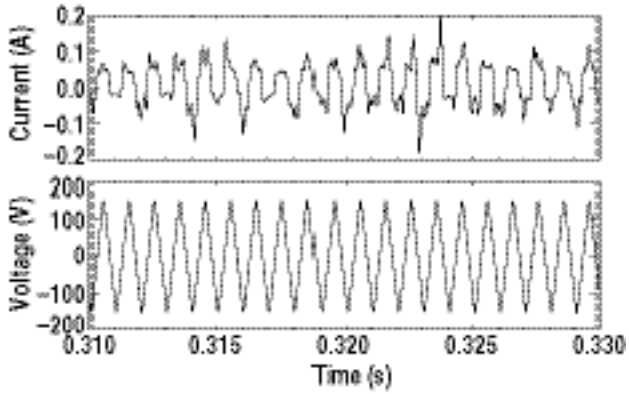

185-06 fig. 15 jy

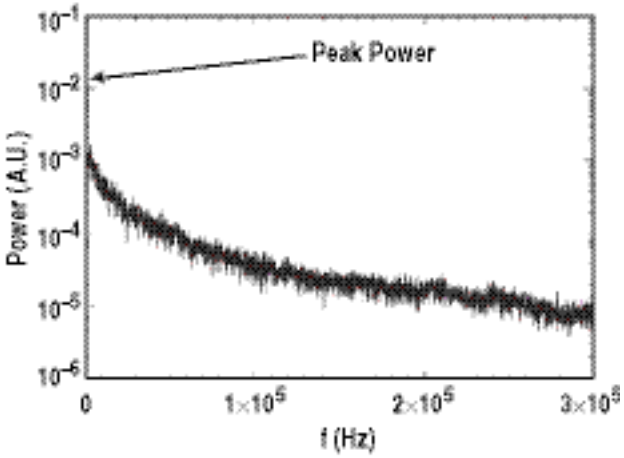

165-06 fig. 16 jy

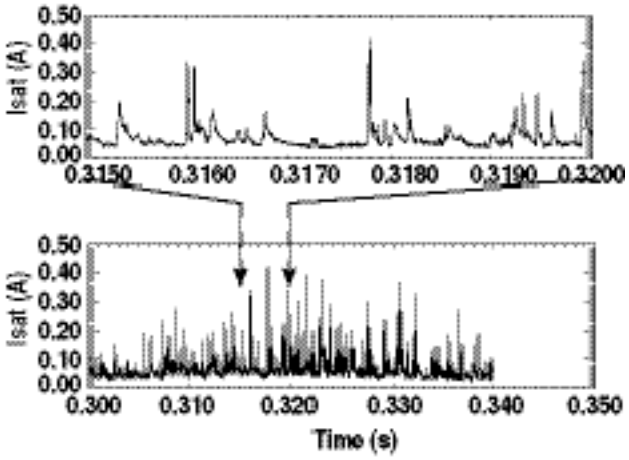

165-06 fig. 17 jy

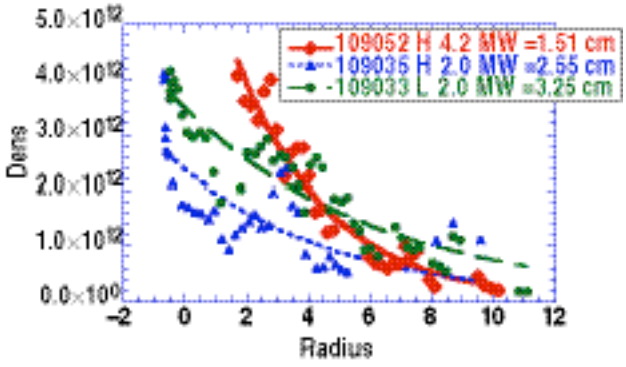

165-06 fig. 18 jy

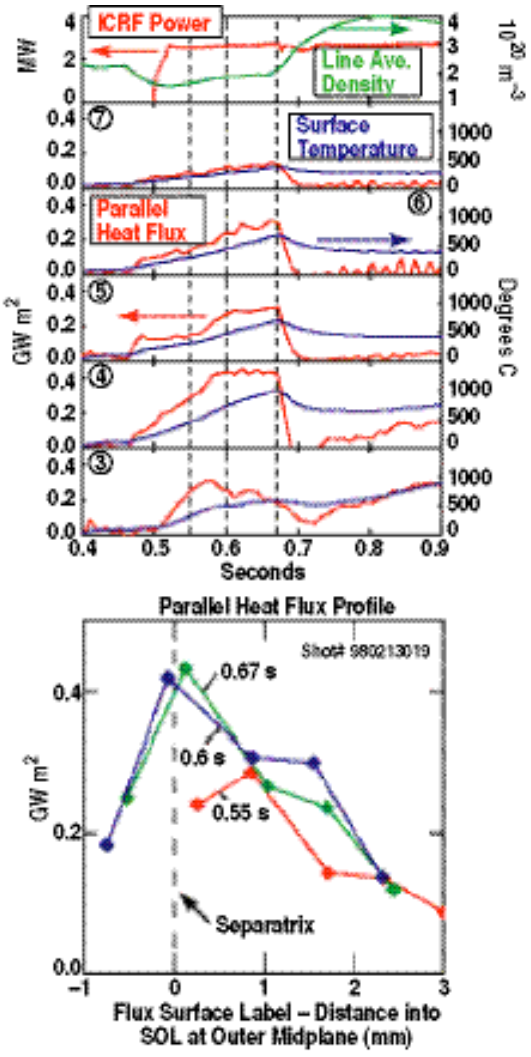

165-06 fig. 19 jy

165-06 fig.3/rs